Z. Phys. C – Particles and Fields 48, 411–431 (1990)

Zeitschrift für Physik C Particles and Fields

Measurement of the inclusive charged-current cross section for neutrino and antineutrino scattering on isoscalar nucleons

P.S. Auchincloss[1], R. Blair[2], C. Haber[3], E. Oltman[3], W.C. Leung, M. Ruiz[4], S.R. Mishra, P.Z. Quintas, F.J. Sciulli, M.H. Shaevitz, W.H. Smith[5]
Columbia University, New York, NY 10027, USA

F.S. Merritt, M. Oreglia, P. Reutens[6]
University of Chicago, Chicago, Il 60637, USA

R. Coleman, H.E. Fisk, D. Levinthal[7], D.D. Yovanovitch, W. Marsh, P.A. Rapidis, H.B. White
Fermilab, Batavia, Il 60510, USA

A. Bodek, F. Borcherding[8], N. Giokaris[9], K. Lang[10], I.E. Stockdale[11]
University of Rochester, Rochester, NY 14627, USA

Received 26 February 1990

Abstract. This paper reports on measurements of the total cross section for the inclusive reaction $\nu_\mu + N \to \mu^- + X$, as a function of incident energy. Neutrinos and antineutrinos with energy in the range 30–300 GeV were produced in the 1982 Fermilab narrow-band neutrino beamline. A total of 35000 neutrino and 7000 antineutrino interactions were recorded in the CCFR detector located in Lab *E*. The incident neutrino flux was determined by methods similar to those used in previous experiments. The rate of increase with energy of the total cross section (σ/E_ν) in the range 30 to 75 GeV was determined to be $0.659 \pm 0.005(\text{stat}) \pm 0.039(\text{syst}) \times 10^{-38}$ cm^2/GeV and $0.307 \pm 0.008(\text{stat}) \pm 0.020(\text{syst}) \times 10^{-38}$ cm^2/GeV for incident neutrinos and antineutrinos, respectively. The 5.9% systematic errors are due primarily to uncertainties in the flux intensity measurement. The energy dependence of the cross section in the region $E_\nu = 100$–300 GeV was found to be linear, as determined by relative normalization techniques. A weighted average of our previous and present measurement for the total $\nu - N$ cross section yields:

$$\sigma(\nu N) = 0.666 \pm 0.020(\text{statistical} + \text{systematic})\, E_\nu\, 10^{-38}\ \text{cm}^2;$$
$$\sigma(\bar{\nu} N) = 0.324 \pm 0.014(\text{statistical} + \text{systematic})\, E_{\bar{\nu}}\, 10^{-38}\ \text{cm}^2.$$

I Introduction

Neutrino nucleon scattering experiments have provided clear evidence for nucleon substructure. A linear rise of the total cross section with the incident neutrino energy in the range 3–300 GeV implies that the neutrinos interact with nearly free, pointlike constituents of the nucleon. Although results from several experiments indicate that the cross section's energy dependence is linear, there have been discrepancies in the value of the constant of proportionality. This quantity, $\alpha^\nu = \sigma^\nu / E_\nu$ sets the scale for the normalization of parton fractional momentum distributions (i.e., structure functions) and for a determination of the mean square charge of the partons (in conjunction with charged lepton-nucleon scattering data).

Values of α^ν reported by several groups since 1975 are listed in Table 1. By 1983, two similar experiments – CDHS [1d] and CCFRR [1k] – had found mean values of α^ν differing by about 10%. The CCFRR measurements [1k] were obtained from data taken in a dedicated run (E616), specifically designed to measure the normalized cross sections. The CDHSW collaboration repeated the experiment with significant modifications in the flux measurement and analysis, and, in 1985, reported new results [11] which agreed with the higher

Present addresses:
[1] University of Rochester, Rochester, NY 10533, USA
[2] Argonne National Laboratory, Argonne, IL 60439, USA
[3] LBL, Berkeley, CA 94720, USA
[4] CERN, Geneva, Switzerland
[5] University of Wisconsin, Madison, WI 53706, USA
[6] SLAC, Stanford, CA 94305, USA
[7] Florida State University, Tallahassee, FL 32306, USA
[8] Fermilab, Batavia, IL 60510, USA
[9] Rockefeller University, New York, NY 10021, USA
[10] Stanford University, Stanford, CA 94305, USA
[11] University of Cincinnati, Cincinnati, OH 45221, USA

Table 1. Summary of σ^{tot}/E measurements. (The quoted errors are systematic.)

Experiment	Energy range (GeV)	$\sigma^{\nu N}/E$ ($\times 10^{-38}$ cm^2/GeV)	$\sigma^{\bar{\nu}N}/E$ ($\times 10^{-38}$ cm^2/GeV)
CITFR, FNAL (1977) [1a]	40–200	0.61 ±0.03	0.29 ±0.02
BEBC, SPS (1977) [1b]	40–200	0.63 ±0.05	0.29 ±0.03
CDHS, SPS (1979) [1d]	30–200	0.62 ±0.05	0.30 ±0.02
CFRR, FNAL (1980) [1f]	25–260	0.70 ±0.03	
CHARM, SPS (1981) [1e]	20–200	0.60 ±0.03	0.30 ±0.02
BC, FNAL (1982) [1g]	10–200	0.68 ±0.11	
BEBC, SPS (1982) [1h]	20–200	0.66 ±0.03	0.31 ±0.01
Columbia-BNAL (1983) [1j]	10–240	0.63 ±0.05	
CCFRR, FNAL (1983) [1k]	40–225	0.669±0.024	0.340±0.020
CDHSW, SPS (1986) [1l]	10–200	0.685±0.019	0.340±0.009
CCFR (this exp.) [1m]	30–100	0.659±0.039	0.307±0.020

CCCFR value. The new CCCFR results reported here are extracted from more recent data taken in 1982 (E701). These 1982 data were used primarily to search for neutrino oscillations [2a, b]. While the technique was similar to that used in the earlier run (E616), the beam and instrumentation had changed substantially. Since the data-taking was not optimized for the cross section measurements, the errors are somewhat larger, and the results are largely corroborative of the earlier measurements.

The measurement of the total cross section requires an accurate counting of neutrino-nucleon interactions (including acceptance and background corrections), and an absolute measurement of the incident neutrino flux correlated with those interactions. The quantity α^{ν} at fixed E_ν may be written in experimental terms as

$$\sigma^{\nu}/E_\nu = N_{ev}/(\rho_N E_\nu \Phi_\nu), \quad (1)$$

where N_{ev} represents the fully corrected event sample, ρ_N the density of the target in nucleons per cm^{-2}, E_ν the neutrino energy in GeV, and Φ_ν the integrated neutrino flux.

The neutrino energy and flux are determined, using two-body decay kinematics, from measured characteristics of the pion and kaon beam from which the neutrino beam is derived. Hence, precise measurements of the integrated intensity of pions and kaons in the secondary beam during data-taking are necessary. Uncertainty associated with these measurements has, in most experiments, limited the precision of the cross section results. Redundant measurements, employing a variety of methods and hardware, have frequently been performed in the effort to reduce errors. Several of the techniques developed by the CCFR collaboration are described in this paper. The systematic errors in the flux determination are the dominant errors in the results reported here.

II Beamline apparatus and flux monitoring

A. Production of the neutrino beam

The narrow band neutrino beamline is pictured in Fig. 1. In a typical beam cycle, an extracted pulse of the FNAL 400 GeV proton beam ($\approx 10^{13}$ protons per 1 ms pulse) interacts with a beryllium target (1 cm × 1 cm × 33 cm), producing secondary hadrons and leptons. A 60 m chain of magnets and collimators downstream of the primary target selects secondary particles according to charge and momentum. This beam channel was tuned, for the 1982 run, to select positive or negative particles with momentum dispersion $dp/p = 11\%$ (rms) about its nominal setting, p_0, and angular dispersion $\sigma_\theta = 0.2$ mr (rms) about its central axis. The charge and momentum selection reduces the total flux by approximately two orders of magnitude, to 10^{10-11} hadrons per beam pulse, but results in a low-background neutrino beam that is well-defined in energy.

The principal neutrino background is due to mesons which decay prior to final charge and momentum selection, that is, before reaching the entrance to the decay region. This background was measured by running the experiment with the collimator at the entrance of the

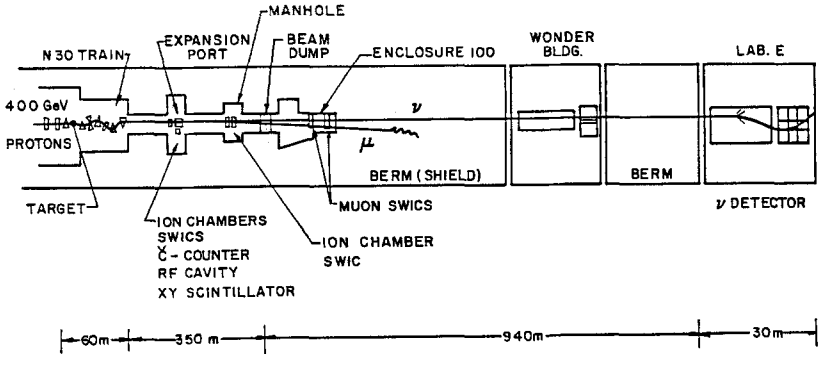

Fig. 1. Schematic of the FNAL neutrino beam line and beam monitoring ports. The figure has not been drawn to scale

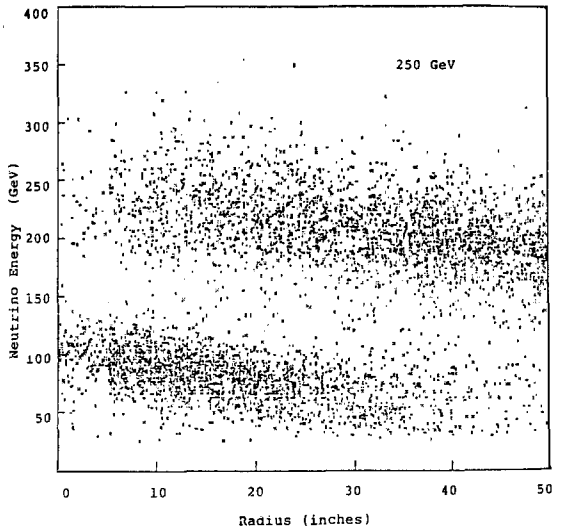

Fig. 2. A representative scatter plot of neutrino energy versus radius of interaction vertex in the detector. The points represented observed events, with neutrino energy measured in the detector

decay region closed. These runs were normalized by using measurements of the primary proton flux.

The secondary beam of protons, kaons, pions, muons and electrons traverses a 352 m long evacuated pipe (the "decay pipe"). Approximately 4% of the pions and 8% of the kaons decay before reaching a 6 m iron beam dump. Muons are stopped in the 940 m earth and iron berm separating the end of the decay pipe and the neutrino detector.

The in-flight decays of the pions and kaons,

$$\pi(K)^{\pm} \to \mu^{\pm} + \nu_{\mu}[\bar{\nu}_{\mu}] \tag{2}$$

produce neutrinos with a strong correlation between energy and direction, as expressed by the following kinematical relation:

$$E_{\nu_{\mu}} = \frac{E_{\pi,K}[1-(m_{\mu}/m_{\pi,K})^2]}{[1+(\gamma_{\pi,K}\theta_{\nu})^2]}, \tag{3}$$

where θ_{ν} is the decay angle of the neutrino with respect to the parent trajectory and $\gamma_{\pi,K}$ is $(E/m)_{\pi,K}$. The upper limit of the neutrino energy is set by the mass of the parent; neutrinos from pion decay have up to 43% of the parent particle energy, and neutrinos from kaon decay up to 96%. The neutrino detector subtends approximately 1 mrad about the central direction. Here, interactions fall into two bands of neutrino energy at any given radius R from the beam axis, as seen in the data of Fig. 2 ($R \approx \theta_{\nu} D$, where D, the distance from the decay point to detector, ranges from 940 m to 1300 m).

Data were collected over a 6 month period at six nominal settings of the secondary beam: 100, 140, 165, 200, and 250 GeV, positive charge; and 165 GeV, negative charge. Approximately 10% of the protons were taken with the final collimator of the beam channel closed, to measure the background due to secondary particles which decayed prior to momentum selection (wide band background). Three days of running were devoted to calibration of secondary beam monitoring devices. For this purpose, a beam of protons extracted at 200 GeV was transported down the entire beam line without a secondary production target. The energy of this beam was known to better than 0.5%.

B. Primary and secondary beam monitoring

Primary beam monitoring. The intensity and lateral position of the primary proton beam were monitored just upstream of the production target. The intensity measurements, obtained principally with a beam current transformer, were used to normalize the closed-collimator (wide band background) data with respect to the regular, open-collimator data. The measurement of the proton flux also played a role in determining the "live" fraction of the neutrino flux, as is described in a later section. The targeting angle of the proton beam, found by a profiling device, strongly influenced the direction of the secondary beam, and therefore was monitored as part of the online beam steering procedures.

Secondary beam monitoring. The principal instruments for monitoring the secondary flux were located in two ports in the decay region. Located in the larger, upstream port, 137 m from the start of the decay pipe, were the following: two ionization chamber assemblies and an rf cavity, all of which measured total beam intensity; a Cerenkov counter used to measure beam composition and mean momentum; a beam profiler (segmented wire ionization chamber, or SWIC); and a transverse scanning scintillator, to cross check the SWIC periodically. The second port, 292 m from the start of the decay pipe, contained a third ionization chamber assembly and a SWIC.

Each of the monitoring devices had an active area which completely contained the beam. The ionization devices were operated with helium gas which flowed through the chambers at atmospheric pressure. The temperature and pressure of the gas in the ionization devices and the Cerenkov counter were recorded as part of the beamline data acquisition system. In addition, the calibration of the digitizing electronics of each device was continuously monitored during the six month data-taking period. Specific features of the principal secondary beam monitoring devices and their use are described in the following paragraphs.

Each of the ionization chamber assemblies, like the one diagrammed in Fig. 3, contained two or more separately digitized charge-collection foils separated by high voltage foils, forming a series of individual chambers. The number, material, thickness, separation and area of the foils varied slightly for each device. All three of the ionization chamber assemblies contained a chamber for measuring the total beam intensity, on a pulse-by-pulse basis. The calibration of these ionization chambers is described in Sect. IV.A. Two of the ionization chamber assemblies, one in each of the monitoring ports, contained pairs of "split-plate" ionization chambers in which top-bottom or left-right halves of the charge collection plane were digitized separately. The ratios (top-

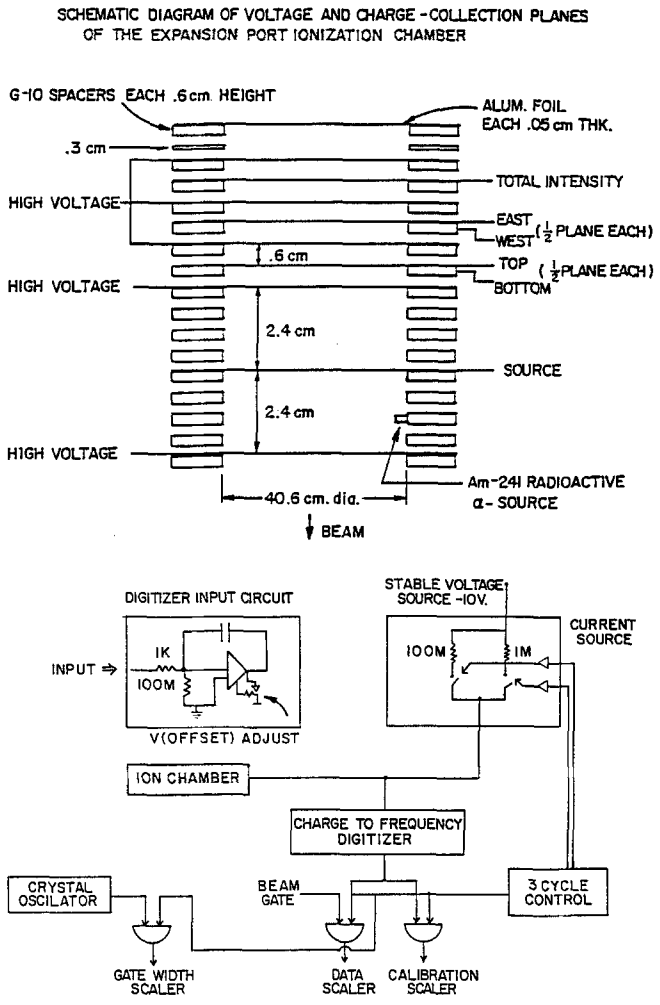

Fig. 3. a A diagram of one of the ionization chamber assemblies, located in the upstream monitoring port. **b** Digitization scheme for the ionization chambers. The right-hand side of the drawing shows the elements of the pulse-by-pulse digitizer calibration. One of three levels of current (0, 0.1, or 10 μA) could be injected into the digitizer during a 1 s period between beam pulses. The stability of the current was controlled by the −10 V source, which was monitored during most of the experiment. The length of the 1 s gate was also measured, as indicated (lower left). After each beam pulse, the calibration reading, voltage monitor, and calibration gate width were recorded, as well as the beam intensity reading and beam gate width. The current sources and the charge-to-frequency digitizers were calibrated after the experiment

bottom)/(top + bottom) and (right-left)/(right + left) were used to stabilize the centre of the secondary beam in the vertical and horizontal directions.

The rf cavity, shown in Fig. 4, was essentially a closed, cylindrical shell folded on itself. The cavity was designed to be responsive to the 53.104 MHz bunched-particle structure of the protom beam (and, consequently, of the secondary beam), which produced an oscillating potential difference in a gap in the inner aluminum wall. Nine resonance studies performed over the course of the experiment, using a variable frequency generator attached at the "antenna" (shown in Fig. 4a), confirmed that the response peaked at or close to the nominal value. The loaded Q value of the cavity was 230. Its impedance was measured to be $6100 \pm 183\,\Omega$, and the ratio of the readout or "tap" voltage to that at the potential gap was 11.75 ± 0.12. The readout electronics of the cavity were upgraded for this experiment with a variable attenuator; this allowed for reproducible adjustment of the overall cavity output as a function of the energy setting.

The Cerenkov counter, shown in Fig. 5, was newly constructed for the 1982 run. This device consisted of an aluminum vessel enclosing an optical frame, which supported the $M1$ spherical focussing mirror (30.5 cm diameter, 305 cm focal length) and the annular iris which accepted Cerenkov light in the angular range 0.7–1 mr. Additional mirrors and lenses served to fold the optical path and direct the light into a photomulitplier tube. An internal shutter was used to measure background due to light not originating in the radiator. Helium gas was used for most of the data-taking, with a 9:1 neon-helium mixture used for the 100 and 140 GeV secondary beam settings. The decoupling of the radiator vessel and the optical frame ensured that the optics would not shift as the counter was pressurized. In taking Cerenkov data, the counter was first aligned and evacuated, and then filled with gas in small increments to a maximum pressure of approximately 1 atm. The light output of the phototube was recorded at each step (once per beam pulse). For consistency checks, at least three, and usually more, Cerenkov runs were taken at each energy setting. Techniques to facilitate background measurement were incorporated into the data-taking procedures (see Sect. IV.B). Runs with a specially extracted 200 GeV primary proton beam were used to calibrate the radiator and study the counter's response to a monoenergetic beam of low angular dispersion and uniform composition.

Each SWIC consisted of a gas-filled chamber containing two planes of charge-collection wires, oriented at right angles to each other and separated by a high voltage plane. The profiles generated by the SWIC data were available to experimenters for each beam pulse. The beam scanning scintillator was $0.6 \times 0.6 \times 1.3$ cm^3 cube of scintillator, suspended from a remotely controlled drive, which permitted movement transverse to the beam direction. Full $x-y$ coverage of the beam with this device took several hours and was done at each beam setting. The resulting scans were used to check the SWIC performance and measurements of beam projections. The scanning scintillator data contained all the $x-y$ correlation information and hence were also of some use in understanding the beam angular dispersion.

Online beam monitoring. As (3) indicates, the angle of the decay neutrino with respect to the secondary beam axis and, consequently, the radial distance R between the event vertex and the beam axis, are closely correlated with the neutrino energy. Considerable effort was therefore made to constrain the lateral drift of the secondary beam. During data-taking, the SWIC's and the split-plate ionization chambers were used as aids in centering the beam; actual corrections were made by adjusting the currents in two pairs of magnets in the beam selection channel. Large shifts, usually caused by mistargeting of

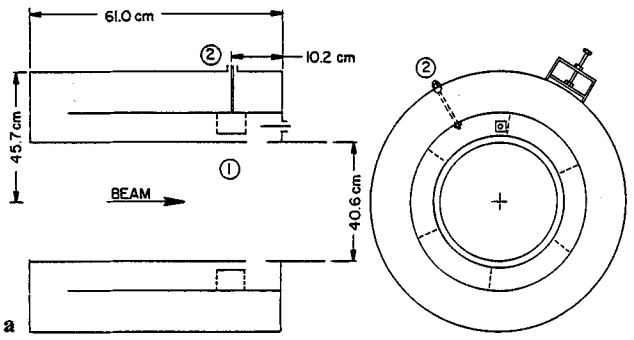

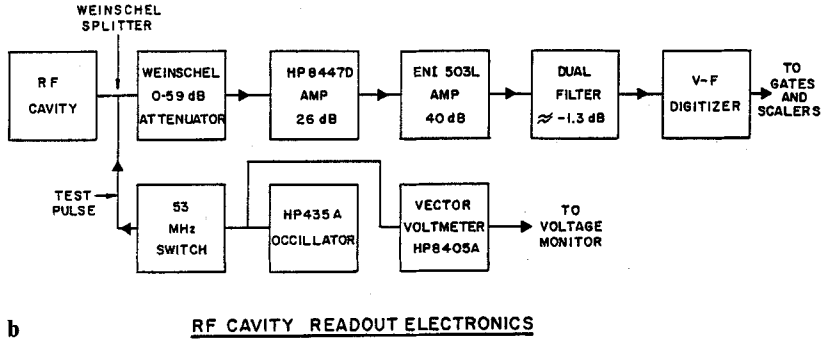

Fig. 4. **a** The rf cavity, side and end-on views. (1) The air "gap" across which an rf potential forms in the presence of a charged particle beam. (2) Voltage "tap" point, at which the voltage is read out. (3) An antenna by which the cavity could be excited from a standard (nonbeam) source, in resonance studies. **b** Electronic circuit for processing the rf cavity output voltage. The variable attenuator permitted adjustment of the digitized output according to the secondary beam setting. Other elements of the circuit, including cables, attenuated the response; the amount of attenuation is indicated *db*. The figure also indicates the point of input of a test pulse, used to check the stability of the readout electronics between beam pulses, and its voltage monitor

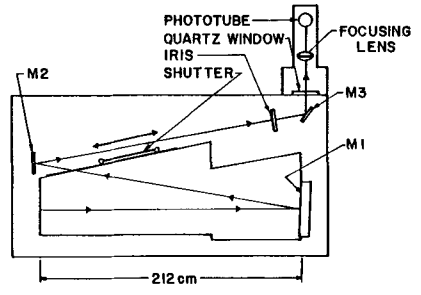

Fig. 5. The Cerenkov counter used in experiment E701. The beam enters from the left. The shutter is used to measure the background from sources outside the Cerenkov radiatative volume

the proton beam, were detected by the profiler upstream of the primary target and were corrected by intervention of the accelerator staff. In the offline data analysis, cuts on the split-plate readings removed both events and corresponding flux for pulses in which the beam center at the detector was outside a ± 2.5 cm window. These cuts removed about 7% of the total data sample.

III Detection apparatus and event collection

The azimuthal symmetry of observed neutrino interactions was reflected in the upstream, unmagnetized, target section of the neutrino detector, which is illustrated in Fig. 6. The fiducial target consisted of 70 steel plates, $3 \times 3 \times 0.05$ m^3, instrumented with 35 liquid scintillation counters (one counter after every two plates) and 16 spark chambers (one chamber after every four plates). The rms hadronic energy resolution $0.89/\sqrt{E(\mathrm{GeV})}$, was measured directly using a hadron test beam two years prior to the 1982 run [3]. This value was confirmed in the analysis of these narrow band neutrino (E701) data. The spatial resolution of the spark chambers was ± 0.5 mm. The fiducial mass of the target, including all components (steel plates, counters and chambers), was 3099.2 g cm^{-2} or 1.8663×10^{31} nucleons·cm^{-2}. The density of each steel plate was measured and the mean value agreed with the standard density to within 0.25%.

The 17 kG toroidal magnet in three segments which followed the target was similarly instrumented with plastic scintillation counters and spark chambers. As a muon spectrometer, the toroid provided an average transverse momentum kick of 2.4 GeV/c to a particle traversing all three segments. The rms fractional momentum resolution was $\sigma_p/p = 0.11$. Three trigger counters were positioned within the spectrometer, and a veto counter was located at the upstream end of the apparatus.

The class of interactions between neutrinos and nucleon constituents which are mediated by the charged

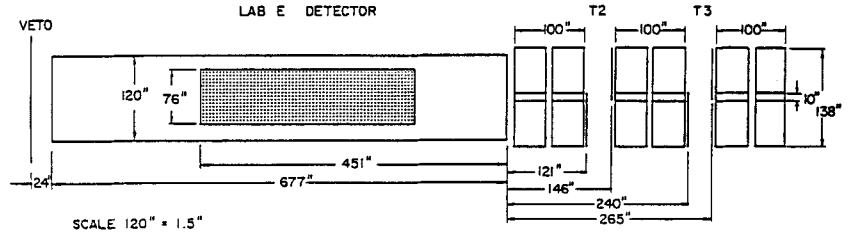

Fig. 6. The neutrino detector in Lab *E*. Dimensions are given in inches. The shaded region represents the fiducial volume in which the observed neutrino events were accepted. The three toroidal segments of the muon spectrometer comprise the downstream end (right-hand side) of the detector

weak boson W^+ produce a single lepton and hadronic fragments, the latter being undifferentiated in an inclusive study. These "charged-current" events from muon neutrinos can be identified by the straight muon track emerging from the shower of hadronic energy deposited near the interaction vertex. The radius R of the interaction point, in combination with energy information (see Fig. 2), is sufficient in most cases to classify the interacting neutrino as originating from pion or kaon decay. (Classification by parent type is crucial to flux normalization and determination of the neutrino energy; see Sect. V.) Energy information comes from observation of the hadronic shower with the target calorimeter and from measurement of the momentum of the outgoing muon with the spectrometer. Even without full reconstruction of the muon track, the event can generally be classified using the hadronic energy and the angle of the muon with respect to the beam axis.

Triggers were counted both during the 1 ms beam pulse (every 10–15 s), and during a 10 or 30 ms period between beam pulses to directly measure any cosmic ray background. Two triggers were used in the experiment. For the "muon" trigger, the muon had to pass through at least four consecutive calorimetry counters as well as a trigger counter in the spectrometer (no minimum hadronic energy requirement). Muon trigger events generally had a completely reconstructed muon track and therefore provided total energy ($E_{\mathrm{TOT}}=E_{\mathrm{HAD}}+E_{\mu}+E_{\nu}$) information. A very large fraction (>98%) were actual beam associated neutrino events.

For the "penetration" trigger, a minimum of 3 GeV of hadronic energy was required, and the muon had to pass through at least sixteen calorimetry counters (no spectrometer chamber hit required). While E_{TOT} could not be measured for some of the penetration trigger events, the angular acceptance of the penetration trigger greatly extended the kinematic acceptance of observed events to more than 95% of the full range at most beam settings. The type of parent hadron (i.e. pion or kaon decay) of the incident neutrino was determined on a statistical basis [1k] (see Sect. V). The two triggers were electronically independent, but their kinematic overlap facilitated computations of the trigger and reconstruction efficiency. About 80% of the triggered events overlapped both triggers.

The event sample was normalized only to the neutrino flux which arrives while the detector was electronically ready to take data. Deadtime occurred principally due to the 30–50 ms needed to clear residual ions from the spark chamber gaps. This limited the detector to recording one event per beam pulse. Two separate methods of measuring the "live" fraction of the flux were compared. The first method related the "live fraction" to the ratio of the sum of muon triggers observed during the live period to that of muon triggers observed during the entire beam pulse (over a large number of beam pulses). The second method similarly used the ratio of the proton flux measured during the live and total beam pulse periods. This second method was employed as the measure of the livetime beam fraction, since it was better suited to our method of summing and correcting the flux in the ion chambers on a pulse by pulse basis. The two methods (over the six beam settings) agreed on average to about 1%. This was taken to be the error on the livetime fraction measurement.

IV Flux analysis

The goal of the flux analysis, as previously stated, was to evaluate the quantity $(E_{\nu}\Phi_{\nu})\,dR$, the energy-weighted neutrino flux, in annular bins concentric with beam axis ($dR=12.7$ cm) at the detector. The energy and flux were determined separately for the neutrinos originating from pions and kaons in the secondary beam (corresponding to similar classification of the observed neutrino events). Given that the secondary beam approximated a uniform, parallel, monoenergetic set of pions and kaons, from which the neutrino spectrum could be easily calculated, the primary uncertainty in the neutrino flux normalization is due to uncertainty in the number of decaying secondary hadrons. The determination of the secondary hadron flux is in turn directly related to the calibration of the four total intensity monitors and the extraction of particle ratios from the Cerenkov data, described in Sects. IV.A and IV.B, respectively. The radial dependence of the energy-weighted flux was also influenced by the mean momentum of the secondary beam, the measurement of which is discussed in Sect. IV.C. For neutrinos from pion decay, the distribution was sensitive to the pion rms angular dispersion, which was of similar magnitude to the opening angle of the decay neutrino ($1/\gamma_{\pi}$); this is discussed in Sect. IV.D. The $\pm 11\%$ momentum spread of the secondary beam and its finite transverse dimensions were found to have negligible effect on the neutrino spectrum for pion decay neutrinos.

The calculation of the neutrino flux in various energy bins relied on a model of the beam which is discussed in Sect. IV below.

A. Total intensity measurement

Ionization chamber calibration. As noted earlier, readings of the four total intensity monitors were taken every beam pulse. Temperature and pressure information and the online digitizer calibration were used to correct for small shifts in relative calibration over time. Absolute calibrations of the ion chambers were carried out in several settings, which are described below.

(1) Calibration using foil activation: Using special runs with the dedicated 200 GeV proton beam, ionization chamber readings were compared to the results of a copper foil activation. The copper foil was placed in the upstream monitoring port. Both the ionization devices and copper foil were exposed to an integrated intensity of approximately 10^{22} protons. The foil was then analyzed for the amount of copper converted through the reaction $\mathrm{Cu}+p\rightarrow{}^{24}\mathrm{Na}+X$. Calibration errors originate for the uncertainty in the ^{24}Na production cross section [4] ($\pm 4.1\%$) and from the measurements of the foil activity ($\pm 2.6\%$), yielding a total error of $\pm 4.9\%$.

(2) Calibration against an rf cavity: During regular data-taking, the ionization devices were continuously cross calibrated with the rf cavity. In principle, the response of the rf cavity was calculable given a description of the beam microstructure (2 ns-rms pulses every 18 ns), the measured properties of the cavity (its resonance curve, impedance, and tap-to-gap voltage ratio), and the attenuation of the readout electronics. The calibration of the cavity involved a detailed study of the nonlinear output of the electronics at low instantaneous beam intensity, incorporating data at all attenuation settings used in the experiment (see Sect. II). The intensity dependence was then folded into the overall shape of the beam pulse (intensity with respect to time on a 1–2 ms time scale). The resulting calibration function (of beam intensity) thereby achieved was considered accurate to $\pm 4.2\%$, with the main contributions to the error coming from the parametrization of the beam microstructure ($\pm 2\%$), the impedance measurement ($\pm 3\%$), variation among calibrations at different attenuation settings ($\pm 2\%$), and the parametrization of the overall beam shape ($\pm 1\%$).

The ratio of flux measured by the rf cavity to that measured by the ionization devices, when taken as a function of the relative proton component of the beam, confirmed an effect discovered by different means in a previous experiment (E616, 1979–80) [4]. The chamber-to-cavity flux ratio increased linearly with proton fraction, suggesting that the calibration "constant" for the ionization chambers was a linear combination of separate calibration constants for protons and mesons. That is,

$$C_{\mathrm{TOT}} = f_p \cdot C_p + f_m \cdot C_m,$$

where C stands for the calibration constant, f represents particle fraction, and the subscripts p and m designate proton and meson, respectively. The origin of the difference in calibration constants for the two types of particles lies in their respective rates of interaction in the chamber foils and the type and multiplicity of the charged products of these interactions. An enhancement in ionization of 6.5% for protons over mesons was predicted by a simple model. This value is in good agreement with measured 7–9% differences found by plotting the chamber-to-cavity flux ratios, averaged at each energy setting, as a function of proton fraction of the beam. Figure 7 shows the resulting plots together with fits to the above formula rewritten as

$$C_{\mathrm{TOT}} = f_p \cdot (C_p - C_m) + C_m. \tag{4}$$

Based on the fits, a pair of calibration constants for each ionization chamber were incorporated in the total intensity calculation.

(3) Calibration in a low intensity beam using particle counting: This third method of calibration utilized a standard method: the chamber was placed between two hodoscope arrays, the setup was exposed to a beam at intensities compatible with counting particles using scintillator counters ($\approx 10^6$ particles per second), and the ionization current was compared to coincidences in the scintillators. For the E701 experiment, one of the ionization chambers was calibrated in a secondary beam containing protons, pions, and kaons.

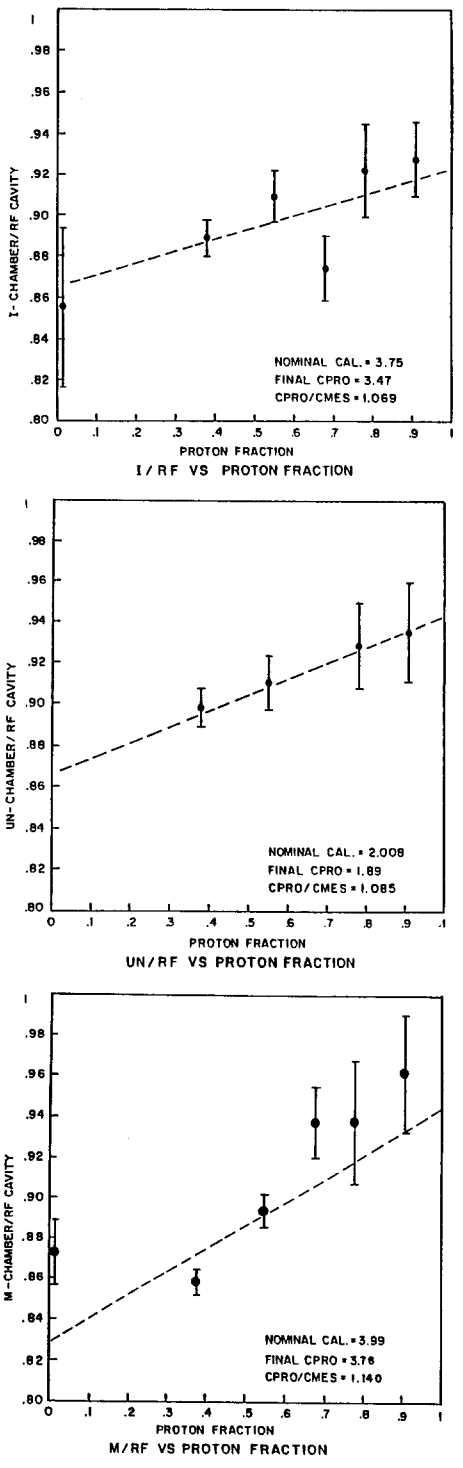

Fig. 7. a–c Plots of the ratio of the three ion chambers' fluxes to the flux calculated with the rf cavity algorithm, indicating variation with primary beam intensity

Data for this calibration were taken at three energy settings, both with and without a thin plate of titanium placed upstream of the chamber. Small corrections were applied to compensate for variations in temperature and pressure, random coincidences, and double occupation

Table 2. Summary of ionization chamber calibration results. The error in each of the calibration techniques was estimated at 5%. However, a check on the level of consistency between the results of the measurements indicates a 7% uncertainty in each calibration, which yields a 5% error on the average value

Method	C_{prot} (pcoul/10^6 particles)
Foil activation	1.952 ± 0.0956
RF cavity	1.890 ± 0.0945; $C_{\text{prot}}/C_{\pi,K} = 1.0848$
Direct calibration	2.187 ± 0.0909; $C_{\text{prot}}/C_{\pi,K} = 1.0848$
Value used (mean)	2.010 ± 0.1000; $C_{\text{prot}}/C_{\pi,K} = 1.0848$

of beam buckets. As in previous studies, no effect due to the presence of the material was observed [4]. The uncertainty in the final calibration constant, after accounting for the difference in proton and meson response, was estimated to be $\pm 5\%$ (rms deviation) based on observed run-to-run fluctuations.

Calibration results. The calibration results for a single chamber are listed in Table 2. The three measurements average to 2.01 pcoul/10^6 particles with a $\pm 5\%$ estimated systematic uncertainty. This error on the ionization chamber calibration dominates the precision of the cross section measurement.

Linearity and stability. The total intensity measurement was complicated by two unforeseen problems. First, the digitizing scalers on the ionization chambers were found to saturate under conditions of high instantaneous beam intensity ($\geqq 10^{13}$ protons in 1 ms, approximately, corresponding to $\geqq 10^{11}$ secondary hadrons in the ion chambers). The rf cavity's output electronics, as mentioned above, were nonlinear at low counting rates ($\leqq 0.5 \times 10^{13}$ protons in 1 ms, approximately, corresponding to $\leqq 0.5 \times 10^{11}$ secondary hadrons). The approach was to use the rf readings at high beam intensity and the ionization chamber readings at low intensity. Cross calibrations between the two types of device were done using data falling in the mid-intensity region common to both.

Second, the ionization chambers exhibited 3–5% shifts in calibration at one point during the run, coinciding with several changes in beam energy and polarity. Whereas the absolute calibration of the cavity was known to $\pm 5\%$, the *stability* of the rf electronics was found to be better than $\pm 2\%$ over the course of the run, as determined by test pulses applied to the circuit beam pulses. Because the rf cavity was relatively stable throughout the experiment, it was used to correct for instabilities in the ionization chambers. An error of $\pm 2\%$ due to the instability was included in the overall systematic error on the cross section.

B. Particle fractions

The determination of pion and kaon beam fractions using data taken with the Cerenkov counter formed the second part of the flux measurement. Since Cerenkov light at a fixed angle is monitored by the phototube, the Cerenkov relation, $\cos\theta_c = 1/(n\beta)$, implies that varying the index of refraction n (by increasing the gas pressure) resolves particles with different β, yielding a mass spectrum of the secondary beam. In principle, the area under each mass peak, after subtraction of backgrounds and accounting for upstream decays, is proportional to the number of particles of each mass.

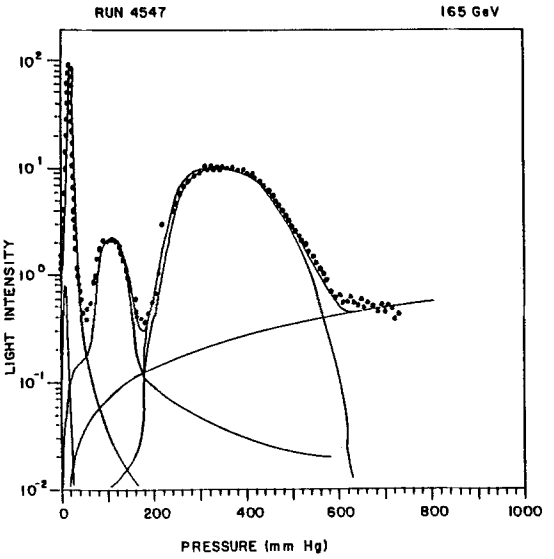

Fig. 8. Cerenkov data and fits at the energy setting of 165 GeV. Shown are the data (dots) after subtraction of the shutter-closed and material backgrounds and the predicted response functions for positrons, pions, kaons, and protons. The residual background function and the sum of the calculated curves are also drawn. The intensity scale in all cases is logarithmic. The extended tail toward high pressure on the kaon peak is due to decay products included in the calculation

The spectrum of 1 mr Cerenkov light with respect to gas pressure, as obtained from the E701 Cerenkov counter, is shown in Fig. 8 at the 165 GeV secondary setting. Data points, after subtraction of known backgrounds, appear as dots on a logarithmic intensity scale. The particle fractions were extracted by fitting the observed spectrum to a calculated spectrum whose composition is indicated by the solid curves in Fig. 8. Curve (a) represents the result of fitting the sum of individual particle spectra and a residual background (see below) to the data points. The individual "response functions", curves (b–d), were calculated using a simulation of the beam that generated Cerenkov light according to the formula [5] appropriate to a Cerenkov counter of finite length L.

$$\frac{d^2N}{d\lambda\, d\cos\theta} = \frac{2\pi\alpha}{\lambda}\left(\frac{L}{\lambda}\right)^2 \frac{\sin^2\psi}{\psi^2}\sin^2\theta \tag{5}$$

$$\psi(\theta) = \frac{\pi L}{2\lambda}[(m/p)^2 + \theta^2 - 2\kappa P] \tag{6}$$

where N is the number of photons emitted at wavelength λ and angle θ by a traversing particle of unit charge. For cases in which $L \gg \lambda/\theta$, this formula reduces to the familiar case. For the 2 m long counter, $L = \lambda/\theta$, the dif-

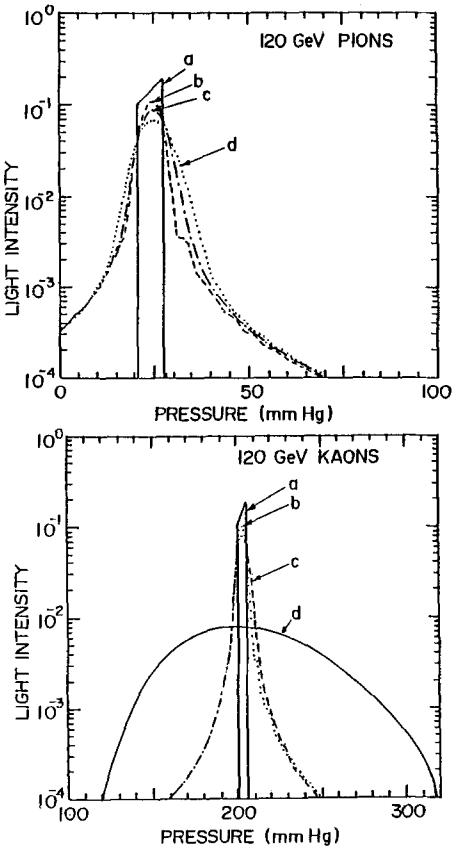

Fig. 9. a, b Calculation of the effects which broaden the Cerenkov pion and kaon peaks under actual beam conditions. (a) The response to an ideal beam (zero momentum and angular dispersion) in an infinitely long counter is broadened only by the finite acceptance (0.7–1 mr) of the iris; (b) diffraction arises when the counter length is set at 2 m; (c) angular dispersion (rms = 0.25 mr) and (d) momentum spread ($dp/p = \pm 0.10$) in the secondary beam broaden the pion and kaon peaks in contrasting ways

fractive effects are substantial. It should be noticed that this formula gives finite light in vacuum, which is expected, and interpreted as transitions radiation. The observation of such transition radiation in this counter has been previously reported [5]. In (6), P is the gas pressure, p is the momentum of the charged particle of mass m, α is the fine coupling constant ($=1/137$), and κ is the gas constant, $\kappa P = n - 1$. The maximum response for a given particle type occurs at pressure

$$P = (1/2\kappa)\,[\theta^2 + (m/p_0)^2]. \tag{7}$$

The widths of the response peaks are influenced by the angular acceptance of the iris, the diffraction of the Cerenkov light, the momentum distribution and angular divergence of the beam particles, and, to a small extent, dispersion in the gas. The relative contribution of each of these effects can be seen in Fig. 9.

The simulated particle spectra incorporated all the above effects and were fitted to the data to determine peak position and width. The ratio of the integrated response of each particle type to the sum for all particle types, after fitting to the data, yielded the particle fraction.

The backgrounds which had to be subtracted from the data or accounted for in the fitting procedure included the following:

Table 3. Particle fractions at the entrance to the decay pipe. Error is the rms deviation among the values found for different runs at given energy setting. (At the negative setting only one run has been used, and the errors have been estimated from the neutrino data.)

Setting	Pion	Kaon	Proton	e/π
100+	0.584 ± 0.005	0.0573 ± 0.001	0.327 ± 0.00	0.054
140+	0.398 ± 0.003	0.0546 ± 0.002	0.542 ± 0.02	0.015
165+	0.287 ± 0.0006	0.0411 ± 0.001	0.667 ± 0.001	0.011
200+	0.188 ± 0.002	0.0278 ± 0.001	0.783 ± 0.000	0.006
250+	0.077 ± 0.002	0.0141 ± 0.0002	0.909 ± 0.002	0.003
165−	0.908 ± 0.010	0.0693 ± 0.004	0.005 ± 0.005	0.02 (err. est.)

(1) Light from sources outside the gas radiator. Photomultiplier readings were taken at each pressure with the main shutter (see Fig. 5) closed. The intensity of this "external" background exhibited a slight linear rise with pressure over the full pressure range. This background was measured and subtracted at each pressure setting point.

(2) Cerenkov radiation from particles produced in beam interactions with material located within approximately three meters of the radiator. Background due to interaction products was measured at each beam setting by placing a 0.95 cm thickness (0.02417 interaction lengths) of aluminum in the beam and recording a full Cerenkov spectrum. The amount of additional light was found to be proportional to the amount of material; therefore, the measured material background spectrum was simply rescaled to the amount of material normally present, 0.0085 interaction lengths. This background was then subtracted from the data at each energy setting.

(3) "Residual" background from unknown sources. Examination of curves after subtracting known backgrounds showed finite amounts of light at high pressures. This residual background is not understood. It was parametrized by examining data obtained with the 200 GeV proton calibration beam. The parametrization, shown in Fig. 8, was included when fitting for the particle fractions. The magnitude of the background appeared to be independent of energy setting, approximately linear with gas pressure, but smaller by a factor of 3–4 for the data taken with the neon-helium gas mixture.

The results of the Cerenkov analysis are tabulated in Table 3. The errors, which come from several sources, are enumerated in Table 4. Notably, the uncertainty in the parametrization of the residual background contributes large errors to the kaon fractions at all settings, but did not significantly affect the pion fractions. The fraction of kaons is characteristically small, and, because the level of the background in the kaon portion of the spectrum is poorly estimated, the relative uncertainty is large. By contrast, errors in the pion beam fraction are less than $\pm 2\%$, owing both to the large fraction of pions in the beam and the location of the pion Ceren-

Table 4. Breakdown of error on particle fractions (in percent). The following are the errors on each particle fraction due to effects mentioned in the text. The total is the sum, in quadrature, of the various errors

Item	100 GeV		140 GeV		165 GeV		200 GeV		250 GeV		−165 GeV	
	π	K	π	K	π	K	π	K	π	K	π	K
CPM linearity	1	1	1	1	1	1	1	1	1	1	1	1
M saturation	1	5	0	0	0	0	1	0	1	0	0	0
CPR linearity	1	0	1	0	1	0	1	0	1	0	1	0
Resid. b.g.	0.3	9[a]	0.2	9.5	0.7	8.0	0.4	4.7	2.4	3.2	0.06	3.3
Reproducibility	0.8	1.7	0.8	3.7	0.2	2.4	1.0	3.6	2.6	2.5	1.1	5.8
Total	1.6	12	1.3	10.2	1.2	8.4	1.8	5.9	3.8	4.2	1.5	7.4

[a] Estimate based on comparison with other curves

Table 5. Comparison of measurements of the mean momentum of the secondary beam. The mean momentum predicted for kaons by the secondary hadron beam model is given in the second column. The values found from the Cerenkov curves and from comparison of observed and predicted mean energy of neutrino events are shown in columns 3 and 4. The quantity p_0 is the average of the measurements in columns 3 and 4, shown with the rms deviation of the two values. The correction factor in the last column was applied to the momentum of each particle-vector of the standard beam model, to produce a momentum distribution with the best estimate as the mean

Setting (GeV)	Beam model p_0 (GeV/c) kaon	Cerenkov p_0 kaon	ν events E_{dat}/E_{pred} study	Best estimate $p_0 \pm$(rms)	Corrections factor
100+	100.6	101.7	106.6	104.2 ± 2.40	1.036
140+	139.8	142.4	144.3	143.4 ± 0.95	1.026
165+	163.6	168.6	169.9	169.3 ± 0.65	1.034
200+	195.0	204.5	201.6	203.0 ± 1.45	1.033
250+	240.9	249.6	247.1	248.3 ± 1.30	1.031
165−	159.8	164.5	163.6	164.2 ± 0.60	1.028

Average error = 0.8%

kov peak in the region of least background. *Therefore, the results for the neutrino cross section are based on the pion neutrino data only.*

C. Mean momentum

For the accurate determination of neutrino flux, the mean momentum of the secondary hadrons is the most significant beam parameter, after integrated intensity. The experiment provided three independent measures of the mean momentum of the secondary beam. Two of these, derived from empirical data were used in the calculation of flux, as described below. The third source was a model of the secondary beam, based on a parametrization of particle production at the primary target [6] and an optical representation of the beam selection channel [7]. Nominal values of the magnet positions, apertures, and currents were used to generate a model of the beam as a set of particle trajectories, distributed in momentum. The mean momentum and angular dispersion of the model secondary beam were adjusted to equal their measured values, as discussed below. This beam model was used in the calculation of the neutrino flux.

To measure the momentum distribution, the individual pressure spectra obtained from the Cerenkov counter were inverted using (5), yielding corresponding momentum curves. The kaon response functions were sensitive to the momentum distribution of the beam (see Fig. 9), but the pion response functions were not. For low masses (m_π, m_e), the width of the Cerenkov peak is determined primarily by the width of iris opening and the beam angular dispersion. The small ($\leqq 1\%$) difference in the mean value of the pion and kaon momenta was derived from the beam model.

The second method of obtaining the mean momentum used events observed in the neutrino detector. A comparison was made between the measured total energy of fully reconstructed events and the same quantity predicted by generating events from the simulated neutrino beam. The kinematic distributions in this case were based on phenomenological quark momentum distributions (Buras and Gaemers [8]) for the parametrization of structure functions. The simulated events were subjected to the same acceptance cuts as the data. The ratio of observed to predicted mean total energies was averaged over 10 radial bins (0–127 cm) for the kaon band events, and over 2 radial bins (0–25 cm) for the pion band events (beyond 25 cm the energy-radius correlation for neutrinos from pion decay is diluted by the angular dispersion for the pion beam).

The results of the two measurements are shown in Table 5, along with the value given by the unadjusted

beam model. The mean momentum was taken to be the Cerenkov value averaged with the corrections found with the kaon and pion band energy studies. The error associated with the final averages at each setting equals the rms deviation among the three input values. The systematic error in the measurement of the mean momentum was therefore approximately $\pm 1\%$, which adds directly into the uncertainty in the value of α^{ν} for pion-band data.

D. Angular dispersion of the secondary beam

Direct measurements of the rms angular dispersion of the secondary beam have proved to be imprecise or unreliable. An alternative was sought in the analysis of E 701. In the method which was finally applied, the angular width of the model beam was adjusted such that the radial distribution of observed and predicted events in the pion band agreed over a large radii (0–127 cm). Although this method used observed events to determine the angular dispersion, little bias was introduced because the energy range of this small number of low energy events was excluded from the cross section analysis. The above indirect measurement of the rms angular dispersion has an estimated uncertainty of $\pm 9\%$. However, since the cross section measurement primarily involves the total flux intensity at each energy setting, the uncertainty in the angular dispersion leads to a systematic error of about $\pm 1\%$ in the pion-band flux normalization.

E. Summary of systematic errors due to flux measurement

The systematic errors in the cross section contributed by measurements of beam characteristics are summarized in Table 6.

Table 6. a Approximate contributions, from flux measurements, to the systematic error on σ^{tot}/E. The values refer to interactions of pion-decay neutrinos within a 30 in radius of the beam center. Note that the actual errors depend on energy setting and position of the interaction in the target

Contribution to error on σ^{tot}/E

Item	E 701 (ν's from π decay)
Ion chamber calibration	5%
Stability and nonlinearity	2%
Pion fraction	1.5%
Secondary beam energy	1%
Secondary beam σ_θ (rms)	1%
Livetime	1.2%
Total	5.9%

V Analysis of neutrino interactions

The essential aspects of the event analysis for the total cross section were the counting of the events and their classification as either pion-neutrino or kaon-neutrino events, depending on the origin of the neutrino.

Classification of the events, as has been mentioned earlier, was simplified by the large energy gap separating the pion and kaon neutrino interactions at each point in radius from the beam axis. If the total energy of the interaction products was known (as for fully reconstructed muon trigger events), the classification was uniquely determined. If only the hadronic energy and muon angle were known (penetration trigger events), classification was still possible on a statistical basis. Details of this technique have been reported in previous publications [1a, k], and are presented briefly here.

Table 6. b Summary of systematic errors (in percent). Statistical errors are also shown, for comparison. Absolute statistical and systematic errors on the total cross section/GeV are given in the last two rows, where the units are those of Table 7

Item	100 GeV		140 GeV		165 GeV		200 GeV		250 GeV		−165 GeV	
	π	K	π	K	π	K	π	K	π	K	π	K
Flux:												
Calib.	5	5	5	5	5	5	5	5	5	5	5	5
RF stability	1.7	1.7	1.7	1.7	1.7	1.7	1.7	1.7	1.7	1.7	1.7	1.7
Nonlinearity	1	1	1	1	1	1	1	1	1	1	1	1
Livetime	1.2	1.2	1.2	1.2	1.2	1.2	1.2	1.2	1.2	1.2	1.2	1.2
f_π, f_K	1.6	12.0	1.3	10.2	1.2	8.4	1.8	5.9	3.8	4.2	1.5	7.4
p_0	1	2	1	2	1	2	1	2	1	2	1	2
σ_θ (rms)	1	0	1	0	1	0	1	0	1	0	1	0
Total Syst.	5.8	13.4	5.8	11.8	5.8	10.2	6.0	8.3	7.0	7.2	5.9	9.4
Events: Stat.	2.2	5.9	1.4	2.5	1.3	1.9	1.4	1.9	1.4	1.2	1-4	3.0
Total syst. & stat.	6.2	14.6	6.0	12.1	5.9	10.4	6.2	8.5	7.2	7.3	6.1	9.9
Absolute errors:												
Stat.	0.014	0.032	0.009	0.013	0.009	0.012	0.009	0.011	0.009	0.008	0.004	0.008
Syst.	0.037	0.073	0.038	0.062	0.040	0.065	0.038	0.049	0.046	0.044	0.018	0.024

Table 7. σ^{tot}/E. Only statistical errors are shown; systematic errors are shown in Table 6b

Setting		Positive polarity		Negative polarity	
		Mean neutrino energy (GeV)	σ^{tot}/E (10^{-38} cm^2/GeV)	Mean neutrino energy (GeV)	σ^{tot}/E (10^{-38} cm^2/GeV)
π	100	40	0.635 ± 0.014		
	140	51	0.665 ± 0.009		
	165	57	0.688 ± 0.009	58	0.307 ± 0.004
	200	65	0.641 ± 0.009		
	250	78	0.650 ± 0.009		
K	100	96	0.546 ± 0.032		
	140	130	0.522 ± 0.013		
	165	150	0.604 ± 0.012	150	0.254 ± 0.008
	200	176	0.596 ± 0.011		
	250	205	0.607 ± 0.008		

The events with hadronic energy higher than the maximum total energy allowed for pion-band events (at given radius) were assigned to the kaon band. Of the remainder, the low angle, high p_μ events also satisfied the muon trigger. After acceptance corrections, the combination of the low angle muon trigger events and the large angle, high E_{had} penetration trigger events provided the rate of kaon neutrino events in all kinematic regions. The contribution from kaon neutrino events was subtracted from the acceptance corrected high muon angle penetration trigger events, yielding the rate of pion neutrino events.

The event sample was corrected for trigger inefficiency, reconstruction inefficiency, detector acceptance, the non-isoscalar target, and backgrounds. These corrections are described below.

After making a set of geometrical cuts defining the fiducial volume of the detector, the acceptance was calculated on an event-by-event basis. The model-independent calculation was based on the longitudinal and azimuthal symmetry of the target volume, the geometry of the detector, and the trajectory of the muon. Essentially, the event vertex was translated in z, and the muon trajectory was rotated through 360° about the beam axis. The reciprocal of the fraction of the translation or rotation for which the event would not pass the acceptance cuts formed the weight of each event. The mean weight of the sample was approximately 1.10.

The efficiency of each trigger with respect to the kinematic quantities E_{had}, θ_μ, and p_μ was computed by comparing the performance of both triggers in regions of overlapping kinematic acceptance. Such comparisons led to the setting of kinematical cuts: for muon trigger events, the requirements were $\theta_\mu \leqq 100$ mr and $p_\mu \geqq 10$ GeV; for penetration trigger events, the requirements were $\theta_\mu \leqq 370$ mr and $E_{had} \geqq 10$ GeV. The momentum cut on muon trigger events eliminated events with low muon momentum for which the efficiency was poor due to energy loss in the target. Corrections for the muon reconstruction inefficiency of about 5% at each energy setting (as determined through hand-reconstruction of 10% of the events) were applied. The hardware efficiency of each trigger was better than 0.99.

The above kinematical constraints placed on the event sample limited the observable kinematic range in $x = Q^2/(2ME_{had})$, the fractional momentum of the interacting quark, and $y = E_{had}/E_\nu$, the fractional energy transferred to the hadronic system, to approximately 95% of the full range. (Here Q^2 is the square of the invariant four-momentum transfer to the target, and M is the proton mass.) This minor acceptance loss was corrected for by calculating the cross section lost in the excluded kinematic regions, using fits to previously measured structure functions [8].

The background contamination due to cosmic ray events was negligible after the application of geometrical cuts. The principal background events were caused by wide-band neutrinos and neutrinos from $K_{\mu 3}$ decay. The wide-band background results from the decay of pions and kaons before momentum selection has taken place in the beam channel. The magnitude and approximate distribution of this background were measured with events collected when the last collimator of the momentum and sign selection beam channel was closed. The number of events observed was scaled by the ratio of the integrated proton flux for open- to that for closed-collimator running. The wide-band subtraction amounted to approximately 5% of the total sample.

Neutrinos from the three body decay of kaons, $K \to \mu + \nu + \pi^0$ ($K_{\mu 3}$ decay), produced legitimate events, but the absence of a unique energy-angle correlation means that some will be classified as pion neutrino events. The number of incident neutrinos from $K_{\mu 3}$ decay (per secondary kaon) was calculated within the overall neutrino flux simulation. The normalization in each annular bin was adjusted for the misassignment of $K_{\mu 3}$ events into the pion band. These $K_{\mu 3}$ corrections were less than 1% because of the small fraction of kaons in the secondary beam.

Finally, the cross section was corrected for the fact that the mostly iron target contained an excess of neutrons over protons. This would lead to an enhancement of the neutrino interaction rate (due to a higher density of d-quarks than u-quarks) and a depletion of the anti-neutrino rate, with respect to a true isocaler target. The final cross section results were multiplied by 0.9755 and

1.0212, for neutrinos and antineutrinos, respectively (corroborated by the measured $\nu-p$ and $\nu-n$ cross sections [10]), to give the cross section for an isoscalar target.

VI Energy dependence of the σ^{ν}/E_{ν}

A. Method of relative normalization

The dominant uncertainty of normalized precision measurements in neutrino interactions has been the flux determination. As pointed out above, the direct flux measurement is difficult, involving as it does a variety of measurements, and employing techniques (such as a Cerenkov counter to determine particle fractions) which have complicated backgrounds. Errors in flux measurements affect both the cross sections and the level of the nucleon structure functions (and, thereby, the measurements of the means square charge of the interacting quarks). An error in the relative flux amoung various energy bins, as well as between neutrino and antineutrino results in altering structure functions F_2 and xF_3, which in turn limits the determination of the QCD parameter Λ_{QCD}. The importance of this can be seen from the new measurements by the CDHSW collaboration [11]; these data, with improved flux monitoring, yield closer agreement with CCFRR cross sections and structure functions than previously published data. It is, therefore, imperative to explore and establish means of normalizing measurements of neutrino interactions which are least prone to systematic uncertainties; and, in principle, can furnish normalizations that only nominally depend upon assumptions involving nucleon structure, i.e. exact scaling or evolution of the nucleon structure functions. An additional motivation to develop new techniques is for optimal use of high statistics precision experiments (having an order of magnitude more events than those using narrow band beams) employing wide band (quadrupole triplet) neutrino beams [13] where direct flux measurement is not feasible.

We argue and adduce evidence here that determination of relative flux may be accomplished by forming appropriate ratios of ν-induced event samples from a specific kinematic region separated into different energy bins and neutrino helicities. Such ratios furnish *relative flux between various energy bins* and *relative flux between* ν_μ *and* $\bar{\nu}_\mu$.

The flux is thus determined *up to one overall normalization constant.* This constant must be obtained from other measurements. In the present case, the π-induced neutrino direct flux measurement is reliable. In a high statistics wide band experiment this can be furnished by the total neutrino or antineutrino cross section obtained independently, or from inverse muon decay events ($\nu_\mu + e^- \to \mu^- + \nu_e$) [13] obtained in the same wide band experiment. We shall briefly outline and contrast three methods of relative flux measurement. We elaborate on the y-intercept technique, used here to obtain the energy dependence of α^{ν} in the E_ν region 100–300 GeV, where events are induced by neutrinos mainly from K-decays. Here the direct flux measurement is inaccurate due to the inadequacy of particle fraction measurements by the Cerenkov counter. This technique has an appropriate balance of statistical and systematic precision for the present application.

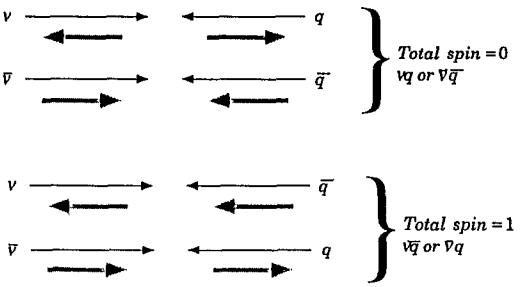

Fig. 10. Helicity representation of neutrino-quark (antineutrino-antiquark) scattering. Single arrows indicate momenta, while double arrows helicity of the interacting fermions

The y-intercept technique. The fundamental premise of this method is that near zero hadronic energy transfer ($y = E_{\mathrm{had}}/E_\nu \to 0$), the differential inelastic cross section divided by energy is a constant, independent of the incident neutrino energy or flavour.

$$\left[\frac{1}{E}\frac{\mathrm{d}\sigma^{\nu}}{\mathrm{d}y}\right]_{y=0} = \left[\frac{1}{E}\frac{\mathrm{d}\sigma^{\bar{\nu}}}{\mathrm{d}y}\right]_{y=0} = \text{constant}. \tag{8}$$

The flavour independence of the above quantity follows from a simple helicity argument (see Fig. 10). The variable y is directly related to the ν-quark centre of mass scattering angle θ^*, $y \approx \frac{1}{2}(1+\cos\theta^*)$. For $y=0$, the helicity differences between ν and $\bar{\nu}$ distinguishing their scattering from quarks (antiquarks) disappear, and only the flavour differences in the target are visible (i.e. charge of the muon). Hence, for scattering from an isoscalar target, (8) should hold up to smearing and radiative corrections [11] (see below).

This point is illustrated more rigorously by considering the $\nu(\bar{\nu})-N$ differential cross section. By invoking the assumptions of locality, Lorentz invariance, CP-invariance, and the $V-A$ current structure of the lepton vertex, the expression of the differential cross section is:

$$\frac{\mathrm{d}\sigma^{\nu(\bar{\nu})}}{\mathrm{d}x\,\mathrm{d}y} = \frac{G_F^2 ME}{\pi}\left[\left(1-y-\frac{Mxy}{2E}\right)F_2^{\nu(\bar{\nu})} + \frac{y^2}{2}2xF_1^{\nu(\bar{\nu})} \pm y\left(1-\frac{y}{2}\right)xF_3^{\nu(\bar{\nu})}\right]. \tag{9}$$

The symbols have their usual meanings; the structure functions F_i are functions of x and Q^2. It should be noted that the above expression is independent of specifics of nucleon composition; in particular no assumption about quark/partons as nucleon constituents need be invoked. We notice that in the limit $y \to 0$, the "y-intercept",

$$\lim_{y\to 0}\frac{1}{E}\frac{\mathrm{d}\sigma}{\mathrm{d}y} = \frac{G^2 M}{\pi}\int_0^1 \mathrm{d}x F_2(x, Q^2 \to 0) = \text{constant}, \tag{10}$$

is independent of neutrino helicity and energy. This argument leads to the procedure of relative normalization

using the y-intercept. At each $\nu(\bar{\nu})$ setting, π or K, the y-intercept is proportional to the appropriate neutrino flux.

$$\lim_{y\to 0}\frac{1}{E}\frac{dN^{\nu(\bar{\nu})}(i)}{dy}=\text{constant}\times\Phi^{\nu(\bar{\nu})}(i). \tag{11}$$

In this equation, $N^{\nu(\bar{\nu})}(i)$ $[\Phi^{\nu(\bar{\nu})}(i)]$ represents the number [flux] of $\nu(\bar{\nu})$-induced events at the i^{th} setting.

The principal practical difficulty in applying (11) is that data are not measured directly at $y=0$, and the structure functions are reliably measured only at higher Q^2 (or y). Therefore, the y-intercept must be extrapolated from higher y. These data (at higher Q^2) are approximately described by

$$\frac{d\sigma^{\nu N}}{dy}=\frac{G^2 ME_\nu}{\pi}[Q^\nu+\bar{Q}^\nu(1-y)^2]\text{ --(a)}$$

$$\frac{d\sigma^{\bar{\nu}N}}{dy}=\frac{G^2 ME_\nu}{\pi}[\bar{Q}^{\bar{\nu}}+Q^{\bar{\nu}}(1-y)^2]\text{ --(b)} \tag{12}$$

in the naive quark-parton model description. While detailed dependence on Q^2 (four-momentum transfer) can in general give, $Q^\nu \neq Q^{\bar{\nu}}$, (10) requires

$$Q^\nu+\bar{Q}^\nu=Q^{\bar{\nu}}+\bar{Q}^{\bar{\nu}} \tag{13}$$

where Q^ν, $\bar{Q}^\nu$, $Q^{\bar{\nu}}$, $\bar{Q}^{\bar{\nu}}$ are defined in (12). Stated in another way, if flux have been correctly determined, we should find

$$\lim_{y\to 0}\frac{d\sigma}{dy}=E_\nu\times b, \tag{14}$$

where b is independent of energy. It should be noted that the application of these techniques using (12) and (14) has four principal limitations:

(1) At very low y, non-perturbative effects, such as quasi-elastic and resonance reactions, will be present which are not well described by (12).

(2) At larger y, there are threshold effects due to charm production. These will be different for ν and $\bar{\nu}$.

(3) There are Q^3-dependent effects which effectively make the Q^ν, $\bar{Q}^\nu$ in (12a) different from $Q^{\bar{\nu}}$, $\bar{Q}^{\bar{\nu}}$ in (12b).

(4) Expressions (12) ignore the effect of a finite value for $R=\sigma_L/\sigma_T$.

We find empirically that a sharp peak occurs for both ν and $\bar{\nu}$ near $y=0$, which could be attributed to the aforementioned quasi-elastic-like processes. This peak is well separated and *not* used for the extrapolation to $y=0$. The effects of items (2), (3), and (4) have been explicitly calculated; the uncertainty of their net effect is estimated to be significantly less than the statistical uncertainty. We describe in detail the application of y-intercept technique below in Sect. B.

Overlapping $x-Q^2$ bins. Comparison of the number of events in a region of x and Q^2 sampled by all energy settings and neutrino flavour provides a consistency check on the relative flux measurement described above [3, 12]. Symbolically:

$$N^{\nu(\bar{\nu})}(i)=f(i)\times\int_x\int_y\int_E\Phi^{\nu(\bar{\nu})}(i)\frac{d\sigma^{\nu(\bar{\nu})}}{dx\,dy}dx\,dy\,dE \tag{15}$$

where $f(i)$ are flux adjustment factors to be determined from this technique. For perfect measurements of $\Phi(i)$, $f(i)$ would be unity. The validity of the method follows from the differential cross section, and the fact that the structure functions ($F_2(x,Q^2)$, $xF_3(x,Q^2)$, and $2xF_1(x,Q^2)$) depend only on x and Q^2. Once these are adequately modeled in the overlapping region of x and Q^2, the $f(i)$'s can be determined. The flux adjustment factors, $f(i)$'s, are largely insensitive to the systematic uncertainties of the model assumptions employed in this technique. Figure 11 shows the dependence of F_2 on x for a wide range of assumptions involving parameters such as the mass of the charm quark ($1.0<m_c<2.0$ GeV), the strange sea content ($0.32<\kappa<0.55$), and $R=\sigma_L/\sigma_T$ (ranging between 01. and the QCD prediction). The effect of these on xF_3 (a nonsinglet structure function) is much less. Since the method employs the *ratio* of integrals over the overlapping regions in x and Q^2, the systematic errors are minimized.

For E616 data, normalized with direct flux measurements, flux adjustment factors were extracted using this method as well as the y-intercept method already described. The results for various beam settings and polarities are shown in Fig. 12a (ν) and 12b ($\bar{\nu}$). The generally

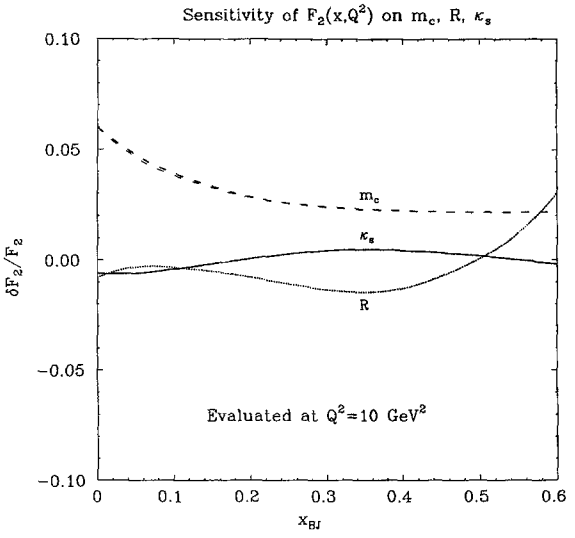

Fig. 11. Sensitivity of the structure function F_2 as induced by various parameters in its extraction from cross sections. The curve marked "m_c" indicates the effect of the uncertainty in the mass of the charm quark: $[F_2(m_c=2.0)-F_2(m_c=1.0)]/F_2(m_c=1.5)$, where the masses are in GeV. In this calculation, the assumed value of the fractional strange sea, $\kappa_s=2\bar{S}/(\bar{U}+\bar{D})=0.5$, where $\bar{Q}=\int_0^1\bar{q}(x)\,dx$. The curve marked "$\kappa_s$" represents, $[F_2(\kappa_s=0.55)-F_2(\kappa_s=0.32)]/F_2(\kappa_s=0.40)$. The curve marked "$R$" conveys the effect due to uncertainty in the R-parameter, $[F_2(R=R_{\text{QCD}})-F_2(R=0.1)]/F_2(R=R_{\text{QCD}})$

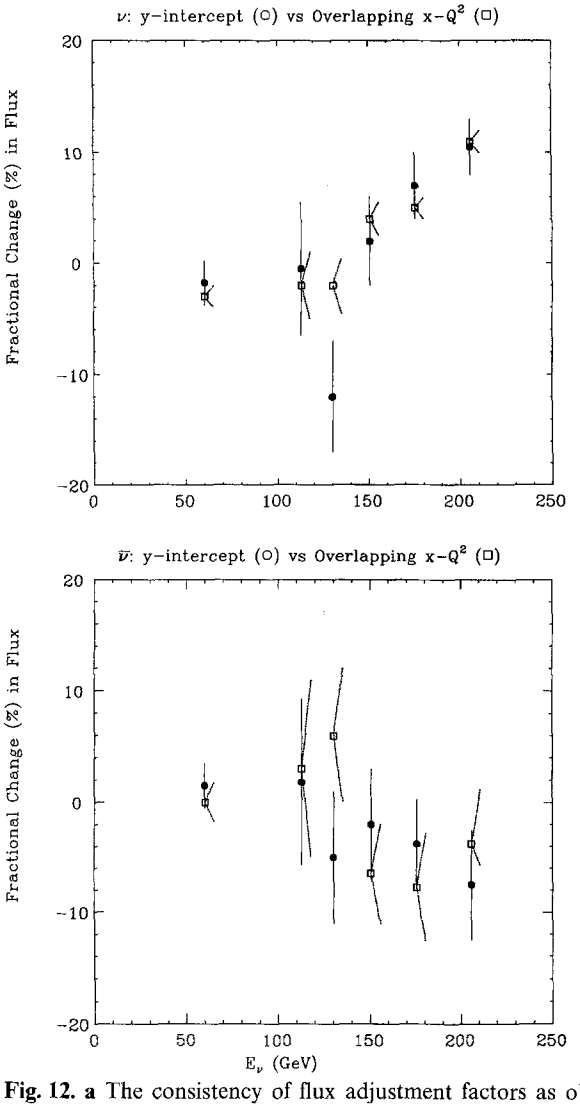

Fig. 12. a The consistency of flux adjustment factors as obtained by y-intercept technique (solid circles) and those from overlapping $x-Q^2$ regions (open squares) using the E616 data. The energies are the average neutrino energies from various beam settings; pion-band neutrinos are plotted as one point. **b** pictures a similar check for the antineutrino data

good agreement reveals the consistency of the two methods. Together they indicate that the direct flux measurement contains a systematic energy dependence which we attribute to measurement of the kaon fraction.

We emphasize that the events employed to extract relative flux using the above two techniques are somewhat statistically independent: y-intercepts are determined mainly from events at low-y (and, hence, at low Q^2), whereas overlapping x and Q^2 method uses only events with large Q^2. In Sect. B, details of the flux adjustment factors obtained from the y-intercept technique are described. In Sect. C, we present the energy dependence of the total neutrino and antineutrino cross section using these factors.

Fixed v_0 method. The dynamics of neutrino-nucleon scattering implies that the number of events in a given energy bin with $E_{\text{had}} < v_0$ is proportional to neutrino (antineutrino) flux in that energy bin *up to* corrections $\mathcal{O}(v_0/E_\nu)$ and $\mathcal{O}(v_0/E_\nu)^2$. This facts permits use of a "fixed v_0 method" for relative flux normalization. We deem it to be systematically the most promising of the three methods enumerated above. It does, however, require a large statistical sample for its application, a situation not amenable in a NBB experiment. We describe the determination of relative flux using this technique in Appendix A.

In Sect. B, we apply the y-intercept technique to our NBB data. We enumerate and estimate sources of systematic errors associated with this method, examine the consistency of the y-intercepts at various settings and polarities. In Sect. C we present the energy dependence of α^ν.

B. *The y-distributions*

The y-distributions were extracted from the pion- and kaon-band event samples at each setting. Since low-y events are of principal interest, only muon triggers were used. The event selection included cuts on the fiducial volume, beam quality and reconstruction, along with requiring muons to have energy greater than 15 GeV and angle less than 150 mr. No hadron energy cut was imposed. Data were corrected for detector geometric acceptance and resolution, and neutrino contamination from $K_{\mu 3}$ decay using a Monte Carlo calculation. Radiative effects do not affect the total cross section, but do modify the shape of y-distribution; hence, radiative correction (following the prescription of de Rujula et al. [11]) was applied at each setting. Finally, isoscalar target corrections were applied to neutrino and antineutrino data. Only data with uniform kinematic acceptance were used. No correction for the kinematic acceptance, charm quark mass and $R=\sigma_L/\sigma_T$ were applied. Effect of these parameters on y-distribution are addressed below.

Figure 13a (pion events) and 13b (kaon events) show the uncorrected y-distributions in the very low-y region. We notice a distinct peak near $y=0$, corresponding to zero E_{had} processes as described earlier. (The $y<0$ events are due to the detector resolution and the subtraction of muon energy deposition [17].) The excess events at very low y show characteristics that are consistent with non-scaling low-E_{had} processes, though asymmetric hadron resolution function also contributes to produce such an effect. The excess above the continuum is larger for the pion data indicating that these scale more nearly with flux $[\Phi(\nu_\pi) > \Phi(\nu_K)]$ than with energy. Nonscaling processes contributing to this region are expected to be (a) quasi-elastic events, $\nu_\mu(\bar{\nu}_\mu)+n(p)\to\mu^-(\mu^+)+p(n)$, (b) resonance production, $\nu_\mu(\bar{\nu}_\mu)+N\to\mu^-(\mu^+)+\mathcal{R}$, where the resonance $\mathcal{R}$ subsequently decays into pions and baryons, and (c) coherent meson production off the nucleus. These processes, collectively referred to as quasi-elastic-like processes (QEP), are expected to be produced equally by high energy ($E_\nu > 15$ GeV) neutrinos and antineutrinos [16]. (There is a small contribution, 0.13% of ordinary charged current interactions, to this region from inverse muon decay reactions.) The typical momentum transfers (Q^2) for these processes are ≤ 1 GeV^2. Follow-

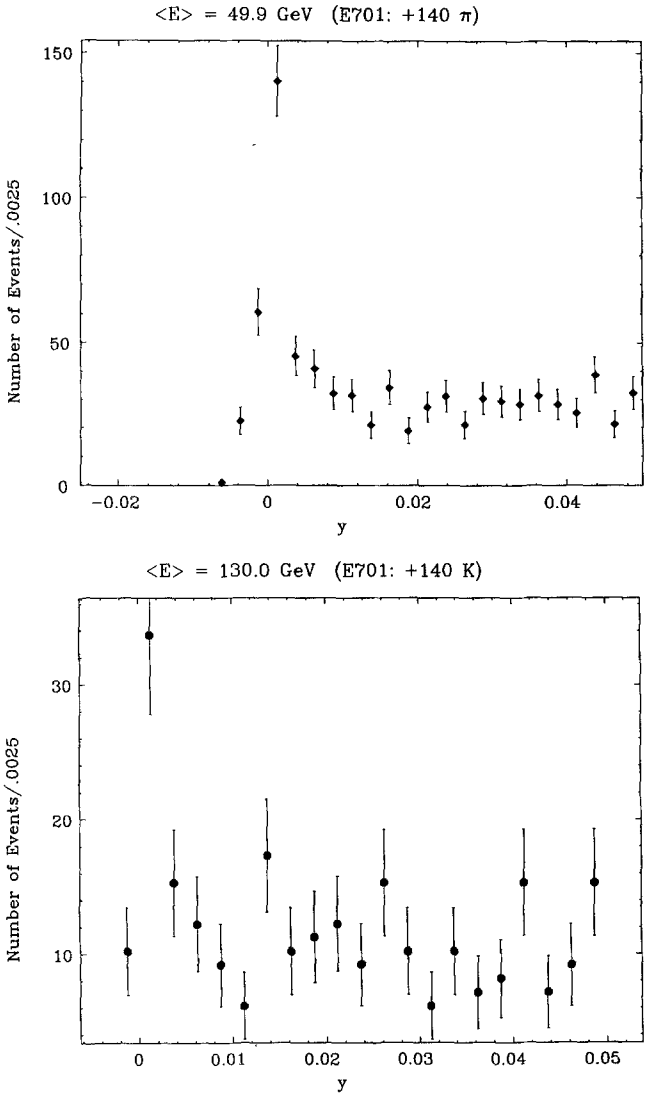

Fig. 13. y-distributions from pion-band **a** and kaon-band **b** neutrinos. The peak at $y=0$, is consistent with non-scaling processes that manifest at very small values of E_{had}; though some contribution due to asymmetric hadron energy resolution is also expected in this region

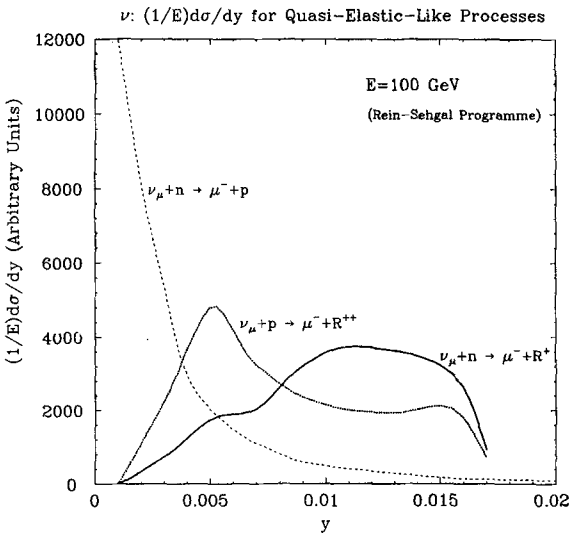

Fig. 14. Simulation of y-distribution due to quasi-elastic-like processes using the formulation of Rein-Sehgal [16]. These include quasi-elastic reactions, and resonance production. The study shows that these processes are confined to small values of y (less than 0.05); and that their cross section is independent of neutrino energy and flavour for $E_\nu > 15$ GeV

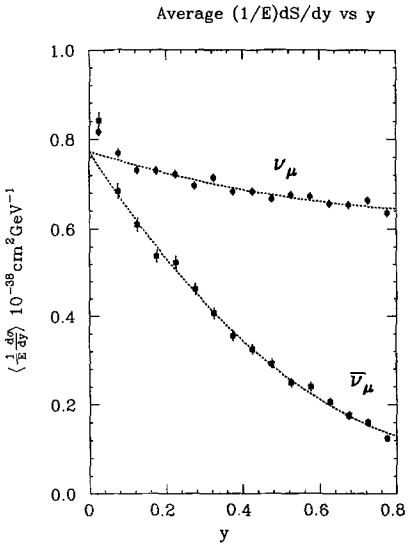

Fig. 15. The cumulative y-distribution for all positive (solid circles) and negative (solid squares) settings after radiative and isoscalar corrections. The fits are to the data in the interval $0.05 < y < 0.8$

ing the Rein and Sehgal formulation [16], these processes were simulated, and were found to lie almost entirely below $y \leqq 0.05$ over the energy regions considered here. Figure 14 illustrates a simulation of $\frac{1}{E}\frac{d\sigma}{dy}$ for QEP events for 250 GeV pion setting: it is seen that the distribution is contained in $y \leqq 0.05$. In the following, the y-distributions were fitted, excluding this lowest bin (i.e. $y \leqq 0.05$), to the simple form given by:

$$\frac{1}{E}\frac{dN}{dy} = A + B(1-y)^2. \tag{16}$$

The y-intercept is given by $(A+B)$; and is extracted in each energy setting. The directly measured flux for the pion band were adjusted using these intercepts; the kaon flux obtained from y-intercepts were used directly. The cross sections, $\frac{1}{E}\frac{d\sigma^\nu}{dy}$, thus obtained, summed over all energy settings, are shown in Fig. 15a for neutrinos (solid circles) and in Fig. 15b for antineutrinos (solid squares) as a function of y. The curves are the summed fits to the data in the interval $0.05 < y < 0.8$. Data above $y > 0.8$ were excluded since these regions have poor geometric and kinematic acceptance. The excess of events in the lowest y-bin ($y \leqq 0.05$) could be due to the forementioned QEP processes, though effects of resolution could also contribute. For each energy setting, the excess of events for $y \leqq 0.05$ over the extrapolated continuum was extracted. Figure 16a (16b) presents the cross section for these

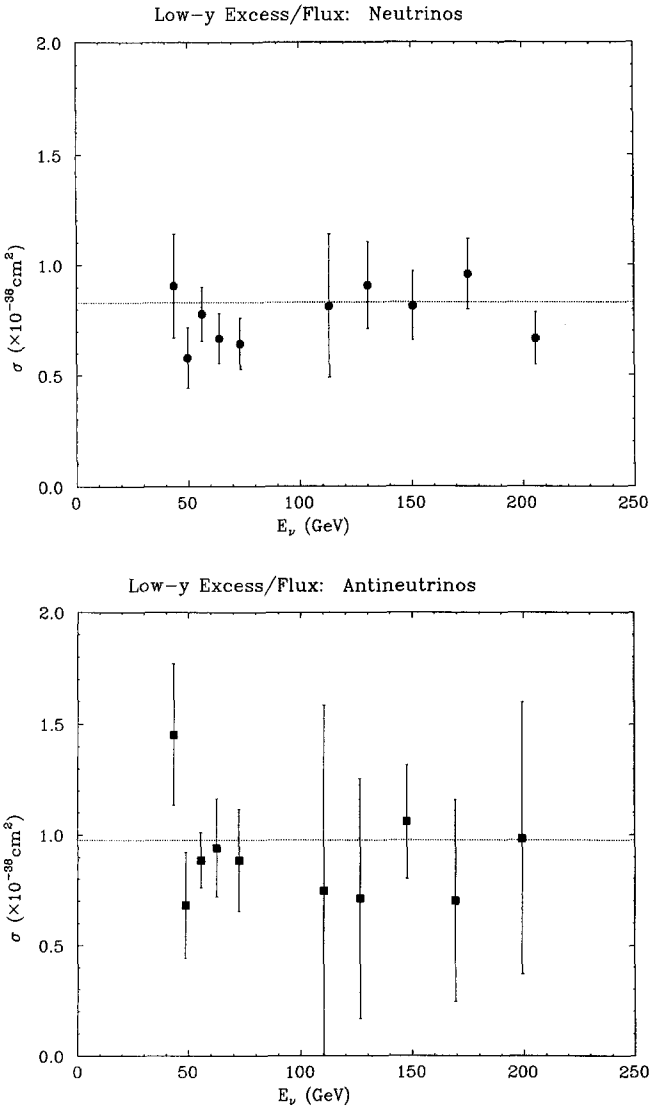

Fig. 16a, b. Empirical evaluation of the cross section of the "excess" events in the lowest y bin ($y \leqq 0.05$) as a function of energy for the neutrino **a** and the antineutrino **b** data. The energy and the flavour independence of these excess are consistent with the QEP

Table 8. a 2-parameter fits to the y distribution in the region $0.05 \leqq y \leqq 0.8$ (low y cut). The errors represent the event statistics only

Setting and polarity		Mean neutrino energy (GeV)	$(10^{-38}$ cm^2/GeV) $(1/E)\,d\sigma/dy$ at $y=0$	$\frac{B}{A+B}$
π	100+	40	0.8389 ± 0.0636	0.4007 ± 0.0805
	140+	52	0.7752 ± 0.0476	0.2339 ± 0.0770
	165+	59	0.8675 ± 0.0468	0.3671 ± 0.0598
	200+	67	0.7235 ± 0.0437	0.1957 ± 0.0782
	250+	77	0.8032 ± 0.0428	0.2760 ± 0.0644
	Weighted average (π^+ set)		0.7960 ± 0.0212	
K	100+	98	0.7049 ± 0.1422	0.1422 ± 0.1860
	140+	130	0.6468 ± 0.0510	0.2679 ± 0.0947
	165+	150	0.8046 ± 0.0494	0.3336 ± 0.0693
	200+	176	0.7290 ± 0.0452	0.2019 ± 0.0786
	250+	206	0.7706 ± 0.0375	0.2486 ± 0.0593
π	165−	58	0.7400 ± 0.0277	0.1146 ± 0.0173
K	165−	147	0.5629 ± 0.0344	0.1865 ± 0.0344

Table 8. b Flux correction factors (with statistical errors) found using the y-intercept method before and after making the cut at low y

Setting and polarity		Mean neutrino energy	Flux correction no low y cut	Flux correction with low y cut
π	100+	40	1.000 (fixed)	1.000 (fixed)
	140+	52	1.000 (fixed)	1.000 (fixed)
	165+	59	1.000 (fixed)	1.000 (fixed)
	200+	67	1.000 (fixed)	1.000 (fixed)
	250+	77	1.000 (fixed)	1.000 (fixed)
K	100+	98	0.855 ± 0.100	0.886 ± 0.124
	140+	130	0.790 ± 0.054	0.812 ± 0.064
	165+	150	0.957 ± 0.050	1.011 ± 0.062
	200+	176	0.874 ± 0.046	0.916 ± 0.057
	250+	206	0.917 ± 0.038	0.968 ± 0.047
	165−	58	1.000 (fixed)	1.000 (fixed)
K	165−	147	0.752 ± 0.040	0.761 ± 0.046

events as a function of E_ν. Within the limited statistical precision, this is flat with energy and the neutrino and antineutrino data agree. The average cross section of the excess is consistent with the ansatz QEP as calculated from Rein and Sehgal [16]; however, the lack of clear theoretical understanding and the ambiguous notion of duality [18] as well as the uncertain effects of resolution, prevents the drawing of a more quantitative conclusion.

The y-intercepts, $\frac{1}{E}\frac{d\sigma^\nu}{dy}_{y=0}$, having removed the lowest y-bin from the fits, were extracted at each energy setting. A weighted average of the values found for the pion-band data was used to determine the scaling constant "b" in (13). Assuming that deviations from this constant in the kaon-band data were due to errors in the original flux normalization, the ratio of y-intercepts $\langle b_K/b_\pi \rangle$ give the factor by which to adjust the respective value of σ_ν/E_ν for the kaon energy settings. The y-intercepts and adjustment factors are listed by energy in Table 8. The adjustment factors are consistent with the errors estimated on the kaon particle fractions (see Table 4). The quoted errors on the cross section values were derived taking into account the correlation between event rate and flux.

A possible systematic error in the y-intercept method could be that the extrapolation to $y=0$ is influenced by processes which affect the shape and level of the y distribution as a function of energy. Although the theoretical basis of the technique is valid at the $y=0$ limit, the extrapolation would be affected by data with $y>0$. Using Monte Carlo generated events, effects which modify the shape of the y distributions were studied both separately and in combination. The calculation began assuming the simple equation (12). Then, charm production was added assuming the threshold mechanism of "slow rescaling" [14]. Next, the study was repeated by including the scaling violation as predicted by QCD

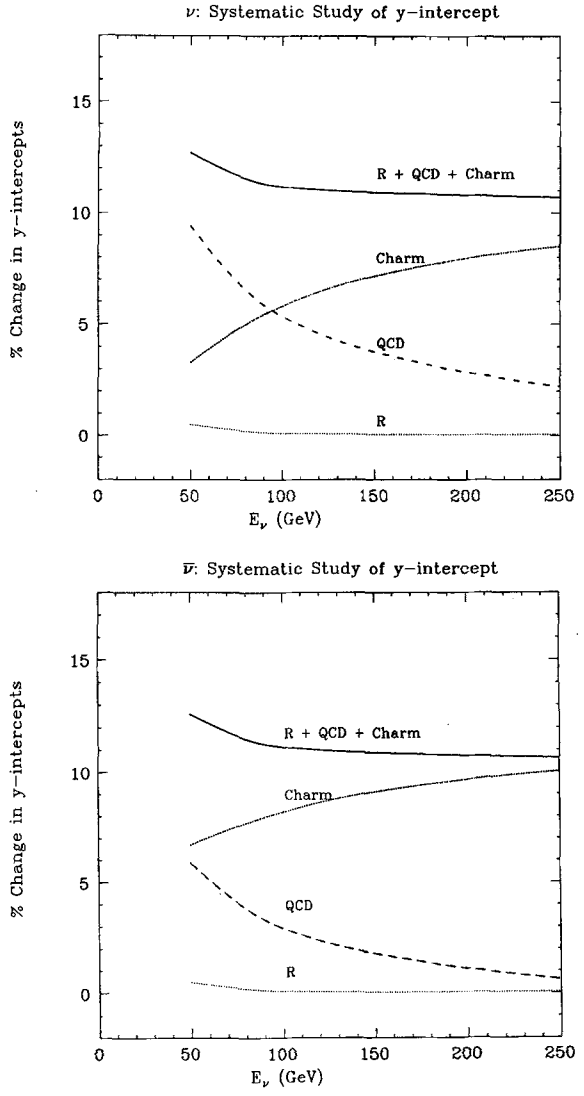

Fig. 17a, b. Energy dependence of y-intercepts due to non-scaling contributions to ν-quark scattering for neutrinos **a** and antineutrinos **b**. The study includes effects of Q^2 evolution of the structure functions, non-zero mass of the charm quark, and the R-parameter

[15]. Here the Q^2-dependence of quark fractional momentum distributions was introduced, using published parameters [3]. Finally, the R parameter was varied amoung the assumptions $R=0$, 0.1, and R_{QCD} [20]. Event distributions were generated for each case and were fitted as for the actual data. The percentage variations of the neutrino (antineutrino) y-intercepts as a function of E_ν are shown in Fig. 17a (17b). When taken alone, each of the former two factors cause deviations of 1%–6% between the y-intercepts at the lowest (50 GeV) and highest (300 GeV) energies. However, in combination, the effects nearly canceled out [12]. The cancellation between the effect of the massive charm quark and the scaling violation can be understood qualitatively: QCD, being an asymptotically free theory, causes the effects of scaling violation to diminish as energy goes up (see Fig. 17). A massive charm quark, on the other hand, would cause the threshold to shift to lower values of y as energy increases, thereby affecting

Table 9. E701 σ^{tot}/E, (a) by direct flux measurements and (b) using relative normalization techniques, by energy setting. The flux correction factors found using the y-intercept method (with low y cut) were used to set the relative normalization. For (a) statistical errors based on the event sample at each setting are given. For case (b) the errors shown are the statistical errors on the flux correction factors

Setting and polarity		Mean neutrino energy (GeV)	(a) σ^{tot}/E direct flux measurement	(b) σ^{tot}/E (in 10^{-38} cm^2/GeV) indirect normalization
π	100+	40	0.635 ± 0.014	(unchanged)
	140+	52	0.665 ± 0.009	(unchanged)
	165+	59	0.688 ± 0.009	(unchanged)
	200+	67	0.641 ± 0.009	(unchanged)
	250+	77	0.650 ± 0.009	(unchanged)
K	100+	98	0.546 ± 0.032	0.616 ± 0.086
	140+	130	0.522 ± 0.013	0.642 ± 0.051
	165+	150	0.604 ± 0.012	0.597 ± 0.037
	200+	176	0.596 ± 0.011	0.651 ± 0.040
	250+	206	0.607 ± 0.008	0.627 ± 0.030
π	165−	58	0.307 ± 0.004	(unchanged)
K	165−	147	0.254 ± 0.008	0.334 ± 0.020

more and more the y-intercepts (since these are very sensitive to variations at low values of y). These two parameters, then, produce opposite effects in the y-intercept. The systematic error resulting from the uncertainty in the mass of the charm quark ($1.1 < m_c < 1.9$ GeV), and from that in Λ_{QCD} (or equivalently various parametrization of the scale-violating structure functions) were estimated from the calculation to be less than 1.5%. Finally, the uncertainty due to the R parameter does not create any appreciable energy or flavour dependence in the y-intercepts. As a result, *no* corrections were applied to y-distributions to compensate for these effects. The cumulative insensitivity of y-intercepts on the parameters support the assumption that the y-intercept remains constant with energy to a level of 1.5% [19].

The overall precision of the y-intercept technique, as a measure of the energy dependence of the cross section, is limited by the statistics of our data sample at low y to a level of 6%–10%, which is comparable to the precision of conventional flux monitoring methods. However, the technique can be applied to data taken with wide band beams, where the statistics at low y are superior.

C. *Results for the energy dependence of* σ^ν/E_ν

The energy-dependence of the cross section, as extracted using the above technique, is summarized in Table 9, and shown in Fig. 18. It should be emphasized that while the low energy points have been normalized using independent measurements of the flux, the high energy points are the result of the comparison of the pion- and kaon-band y-intercepts, and therefore, they reflect the behavior of the cross section *relative* to the low energy points.

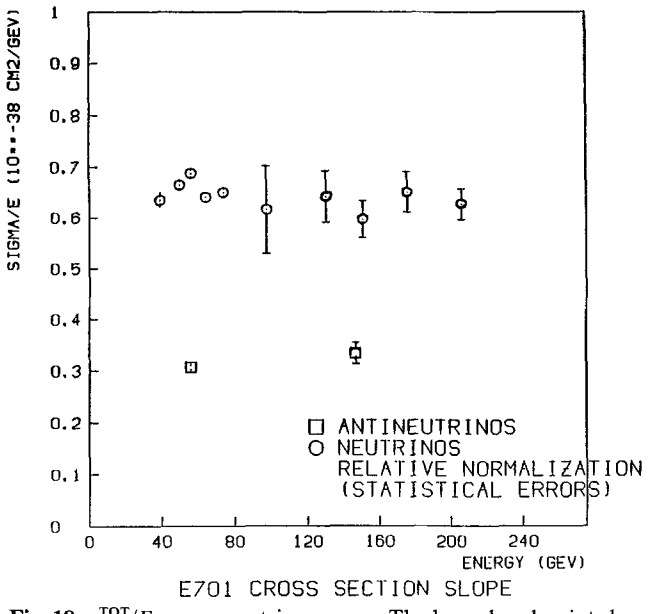

Fig. 18. σ^{TOT}/E versus neutrino energy. The kaon-band points have been normalized relative to the average of the pion-band points, using the y-intercept method. The error bars represent the statistical errors on the y-intercepts

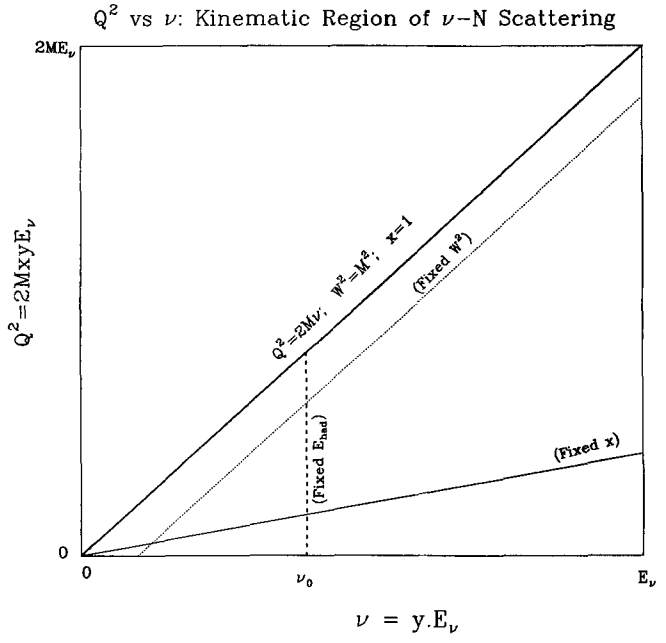

Fig. 19. Q^2 vs $\nu = y \cdot E_\nu$ plot at a fixed E_ν. The kinematic region indicating regions of fixed ν (equivalently E_{had}), x, and invariant hadronic mass, W^2 are shown. From the figure, it follows that (for pure scaling) the ratio of number of events with $\nu_1 < \nu < \nu_2$ at two separate energies is the relative flux between them

The correlated errors incurred in extracting the relative flux using y-intercept are properly taken into account and are included in Fig. 18. A small correction due to the finite mass of the W-propagator has been incorporated in the energy dependence (at the highest measured energy, the magnitude of this correction is 1%). The high energy points have not been included in the final value of α^ν. However, the high energy data indicate that the cross section rises linearly with the incident neutrino energy, in the energy region covered in this experiment.

VII Results for σ^ν/E_ν

The results of the cross section measurement are presented in Table 7. Given the large uncertainty in the fraction of kaons, the kaon flux data and events have not been incorporated into the final determination of α^ν. Nevertheless, the events in the kaon neutrino band, without flux normalization, have been used in a study of the energy dependence of the cross section, as described in Sect. VII.

The final evaluation of α^ν is therefore based entirely on events from neutrinos from pion decay. The events occurred within a 76.2 cm radius of the beam axis. The mean neutrino energy at each setting of the secondary beam is indicated in the table; within a given setting the data span a range of approximately $\pm 5\%$ about the mean. The errors stated are first, statistical, and second, systematic (error due to the flux measurement). The average of the five positive pion settings is

0.659 ± 0.005(statistical)
± 0.039(systematic) 10^{-38} cm^2/GeV.

Most of the systematic errors in Table 6b change the overall scale. The 1.7% error due to fluctuations in the rf cavity is a point-to-point systematic error. A check on the consistency of the cross section slopes from the five neutrino energy settings indicates that there is an additional point-to-point systematic error of 2.5%. This error is negligible when the data from the five energy settings are averaged. However, an additional 2.5% error was added to the systematic error for the antineutrino cross section because data were taken at only one energy setting. The measurement at the 165 GeV negative pion setting yields

0.307 ± 0.008(statistical)
± 0.020(systematic) 10^{-38} cm^2/GeV.

VIII Conclusion

The measurement of the constant of proportionality between the total, charged-current cross section and the incident neutrino energy has been measured to be

0.659 ± 0.005(statistical)
± 0.039(systematic) 10^{-38} cm^2/GeV
for neutrinos, and

0.307 ± 0.008(statistical)
± 0.020(systematic) 10^{-38} cm^2/GeV

for antineutrino scattering on nucleons. These results are based on an analysis of 35000 neutrino and 7000 antineutrino events extending over an energy range $E_\nu = 30$–75 GeV. The incident neutrino flux was determined from measurements of the parent meson beam. These measurements have a systematic error of 5.8%, which

is dominated by the uncertainty in the calibration of the secondary beam intensity monitors. The cross section results closely corroborate those previously reported by our collaboration. A weighted average of our previous and present measurement yields:

$$\sigma(\nu N) = 0.666 \pm 0.020(\text{statistical} + \text{systematic})\, E_\nu\, 10^{-38}\ \text{cm}^2;$$

$$\sigma(\bar{\nu} N) = 0.324 \pm 0.014(\text{statistical} + \text{systematic})\, E_{\bar{\nu}}\, 10^{-38}\ \text{cm}^2.$$

These are in good agreement with recent CDHSW results.

The observed behavior of the σ^ν/E_ν is constant from energies of 30 GeV to 300 GeV. In reaching this conclusion, a technique for normalizing the higher energy kaon-band neutrino events with respect to the absolutely normalized pion-band event sample, was developed and applied. The technique was based on the invariance of the differential cross section, $(1/E_\nu)\,\mathrm{d}\sigma/\mathrm{d}y$, at $y=0$. For our data this technique carries an uncertainty of 6–10% from the statistics of the low y bins. This uncertainty is comparable to conventional flux monitoring methods. Monte Carlo studies indicate that the systematic errors in this technique are on the level of technique for wide band beam data for which the statistics at low y may be better.

Appendix A: fixed ν_0 method

The dynamics of neutrino-nucleon scattering implies that the number of events in a given energy bin with $E_{\text{had}} < \nu_0$ is proportional to neutrino (antineutrino) flux in that energy bin *up to* corrections $\mathcal{O}(\nu_0/E_\nu)$ and $\mathcal{O}(\nu_0/E_\nu)^2$. The determination of relative flux using this technique is pictorially illustrated in Fig. 19, which maps the kinematic relation between Q^2 and ν, evincing the premise of this method. It essentially follows from the expression of the differential cross section (9). Using $\nu = E_\nu \cdot y$, and integrating (9) with respect to x (from 0 to 1) and ν (from 0 to ν_0), we get:

$$\mathcal{N}(\nu < \nu_0) = \Phi(E_\nu) \cdot \int_0^{\nu_0} \int_0^1 \frac{\mathrm{d}\sigma}{\mathrm{d}x\,\mathrm{d}\nu}\,\mathrm{d}x\,\mathrm{d}\nu$$

$$= C \cdot \Phi(E_\nu) \cdot \left[(\nu_0 - \nu_0^2/2E_\nu)\,\mathscr{F}_2 + \frac{\nu_0^3}{6E_\nu^2}\,\mathscr{F}_1 \pm \left(\frac{\nu_0^2}{2E_\nu} - \frac{\nu_0^3}{6E_\nu^2} \right) \mathscr{F}_3 \right]$$

where $\mathscr{F}_i = \int_0^1 \int_0^{\nu_0} F_i(x)\,\mathrm{d}x\,\mathrm{d}\nu$, $\mathcal{N}(\nu < \nu^0)$ is the number of events in a given energy bin (E_ν) with hadronic energy less than ν^0, C is a constant, and the term $\frac{Mxy}{2E_\nu}$ has been suppressed for simplicity. By rearranging terms as coefficients of (ν/E_ν) and its powers we arrive at the more amenable form:

$$\mathcal{N}(\nu < \nu^0) = C \cdot \Phi(E_\nu) \cdot \nu_0 \left[\mathscr{F}_2 - \frac{\nu_0}{2E_\nu}(\mathscr{F}_2 \mp \mathscr{F}_3) + \frac{\nu_0^2}{6E_\nu^2}(\mathscr{F}_2 \mp \mathscr{F}_3) \right]$$

$$= C \cdot \Phi(E_\nu) \cdot \nu_0 \left[\mathscr{A} + \left(\frac{\nu^0}{E_\nu} \right) \mathscr{B} + \left(\frac{\nu^0}{E_\nu} \right)^2 \mathscr{C} + \mathcal{O}\left(\frac{\nu^0}{E_\nu} \right)^3 \right]$$

where we have assumed, for simplicity, the Callan-Gross relation $F_2 = 2xF_1$. The number $\mathcal{N}(\nu < \nu_0)$ is the proportional to the flux upto correction factors of the order $\mathcal{O}(\nu_0/E_\nu)$ or smaller, which are not significant for small values of ν_0 at higher energies. It should be pointed out that the coefficients $\mathscr{A}$, $\mathscr{B}$, and $\mathscr{C}$ are determined for each energy bin and neutrino flavour with the data itself. The insensitivity of this method to various parameters, in particularly to the low-ν region where nonscaling processes contribute, makes it an attractive means of obtaining relative flux. We need high statistics samples in order to used this method effectively. This is met by the quadrupole triplet experiments. The details of this method and the sequent systematic studies will be presented elsewhere [21].

Acknowledgements. We express our gratitude for the skilled and dedicated efforts of the Fermilab staff, in particular, the Neutrino Crew members. We thanks Drs. K. Jenkins, R. Pitt, S. Pordes and D. Owen for their contributions to the flux monitoring. This research was supported by the National Science Foundation and the U.S. Department of Energy.

References

1. a. B.C. Barish et al.: Phys. Rev. Lett. 23, (1977) 1415; b. P.C. Bosetti et al.: Phys. Lett. 39 (1977) 1595; c. A.E. Asratian et al.: Phys. Lett. 70B (1977) 273; d. J.G.H. de Groot et al.: Z. Phys. C Particles and Fields 1 (1979) 143; e. M. Jonker et al.: Phys. Lett. 99B (1981) 265; Erratum 100B (1981) 520; f. J. Lee: Ph. D. thesis, Caltech (1981); g. T. Kitagaki et al.: Phys. Rev. Lett. 49 (1982) 98; Phys. Rev. Lett. 45 (1980) 955; h. P.C. Bosetti et al.: Phys. Lett. 110 (1982) 167; i. G.N. Taylor et al.: Phys. Rev. Lett. 51 (1983) 739; j. N.J. Baker et al.: Phys. Rev. Lett. 51 (1983) 735; k. R. Blair et al.: Phys. Rev. Lett. 51 (1983) 5; l. P. Berge et al.: Z. Phys. C – Particles and Fields 35 (1987) 443; m. P.S. Auchincloss: Ph. D. thesis, Columbia University (1987)
2. I. Stockdale et al.: Phys. Rev. Lett. 52 (1984) 1384; I. Stockdale et al.: Z. Phys. C – Particles and Fields 27 (1985) 53
3. D. MacFarlane et al.: Z. Phys. C – Particles and Fields 26 (1984) 1
4. R. Blair et al.: Nucl. Instrum. Methods 226 (1984) 281
5. A. Bodek et al.: Z. Phys. C – Particles and Fields 18 (1983) 289
6. A. Malensek et al.: Fermilab FN-341 (1981)
7. D.C. Carey: SLAC-0246 (1982); FN-247, Fermi National Laboratory (1972)
8. A. Buras, K. Gaemers: Nucl. Phys. B132 (1987) 249
9. The estimate of the quasielastic cross section was made by integrating the expression for the differential cross section with respect to Q^2, this expression being stated in several articles, for example, T. Kitagaki et al.: Phys. Rev. D28 (1983) 436
10. D. Alasia et al.: Nucl. Phys. B239 (1984) 301
11. A. de Rujula et al.: Nucl. Phys. B154 (1979) 394
12. P.S. Auchincloss et al.: Proc. 12th Int. Conf. on Neutrino Physics and Astrophysics, Sendai, p. 351, T., Kitagaki, H. Yuta (ed.) (1986)

13. S.R. Mishra et al.: Phys. Rev. Lett. 63 (1989) 132
14. H.E. Fisk, F. Sciulli: Ann. Rev. Nucl. Part. Sci. 32 (1982) 499
15. G. Altarelli, G. Martinelli: Phys. Lett. 76B (1978) 89
16. D. Rein, L.M. Sehgal: Ann. Phys. 133 (1981) 79; Nucl. Phys. B223 (1983) 29; D. Rein: Z. Phys. C35 (1987) 43; R. Belusevic, D. Rein: Phys. Rev. D38 (1988) 2753
17. Events with $E_{had} < 0$ result from the detector resolution at small values of E_{had}. Hadronic energy is obtained by summing counter pulse heights. This summation entails a small subtraction of the muon contribution to the shower region. The subtraction, however, dominates the resolution at small E_{had}, occasionally smearing events to negative values. The resolution function for zero E_{had} processes was extracted from straight through muons originating in the earth shield upstream of the detector. This resolution function, subsequently, was used to investigate the excess events in the low-y region. For details see, W.K. Sakumoto et al.: Calibration of CCFR target calorimeter, UR-1142, 1990; submitted to Nucl. Instrum. Methods
18. E. Bloom, F. Gilman: Phys. Rev. Lett. 25 (1970) 1140
19. E. Oltman et al.: Nucleon structure functions from high energy neutrino-nucleon interactions. Invited talk presented at DPF'88, Storrs, Conn., 1988, Nevis-R-1417. To be submitted to Z. Phys. C – Particles and Fields
20. S.R. Mishra, F.J. Sciulli: Ann. Rev. Nucl. Part. Sci 39 (1989) 259
21. P.Z. Quintas et al.: in preparation